Smart Rubber Balloon Dam for Coastal Hurricane and Tsunami Protection: A Renewable Energy-Powered System with Hydrodynamic Design and Adaptive Control

Najah M. L. AL Maimuri

Building and Construction Techniques Engineering Department,
College of Engineering and Engineering Techniques, Al-Mustaqbal University, 51001, Babylon, Iraq.

**Corresponding author: najah.mahdi@uomus.edu.iq
ORCID: https://orcid.org/0000-0002-7752-4182

Ali Abdul Razzaq Altahir

Electrical and Electronic Engineering Department,
College of Engineering, University of Kerbela, Karbela 56001, Iraq.
E-mail: ali.altahir@uokerbala.edu.iq
ORCID: https://orcid.org/0000-0002-8125-6600

Layth Abdulameer

Department of Civil Engineering, College of Engineering, University of Kerbala, Karbala 56001, Iraq. E-mail: laith.saeed@uokerbala.edu.iq

Farhan Lafta Rashid

Petroleum Engineering Department, Kerbela University, Kerbela 56001, Iraq. E-mail: farhan.lefta@uokerbala.edu.iq ORCID: https://orcid.org/0000-0002-7609-6585

Ahmed N. Al-Dujaili

Petroleum Engineering Department,
Amirkabir University of Technology, No. 350, Hafez Ave, Valiasr Square, Tehran, Iran.
E-mail: ahmed.noori203@aut.ac.ir
ORCID: https://orcid.org/0000-0003-0509-4504

(Received on April 12, 2025; Revised on June 14, 2025 & August 16, 2025; Accepted on September 1, 2025)

Abstract

The Coastal regions are increasingly vulnerable to hurricanes and tsunamis, which cause severe damage to infrastructure and communities. Traditional barriers such as seawalls and breakwaters are rigid, costly, and often ineffective under extreme hydrodynamic forces. This study proposes a smart rubber balloon dam as a flexible, rapidly deployable, and renewable-energy-powered alternative for coastal protection. The system consists of elliptical inflatable balloons anchored in underground trenches along the shoreline. Balloons are inflated using compressed air supplied by an air storage tank, powered by a Horizontal-Axis Wind Turbine coupled with a Doubly Fed Induction Generator, and supported by deep-cycle batteries. To ensure precise operation, a backstepping controller regulates the three-phase induction motor driving the air compressor, achieving a 95% reduction in rotor speed tracking error and settling time of less than 0.5 s. Balloon inflation pressure is stabilised by an Adaptive Neuro-Fuzzy Inference System, which reduces transient variations by 70% and maintains a pressure stability of ±5 % under dynamic hydrodynamic loads. The system was validated through Simulink modelling and hydrodynamic analysis, including case study forces derived from the 2004 Sumatra tsunami. Results confirm reliable balloon deployment, consistent rigidity against bore wave action, and renewable energy self-sufficiency, with 85% conversion efficiency and a stable 4.8 kW output across wind speeds. Compared to conventional defenses, the proposed system offers a faster response, greater adaptability, and a lower environmental impact. This research highlights a novel AI-powered, renewable energy-integrated coastal defense strategy that provides a scalable,



sustainable, and climate-resilient solution for shoreline protection. The Adaptive Neuro-Fuzzy Inference System controller achieves consistent balloon rigidity even under dynamic contact loads, reducing transient variations by 70% while maintaining pressure deviations of less than 5% from the setpoint.

Keywords- Tsunami mitigation technology, Smart rubber balloon, Smart actuation systems, Coastal hurricanes, Inflatable coastal defense, Alternative energy, Renewable energy integration, Hydrodynamic design, Backstepping control.

Abbreviations

AI Artificial Intelligence

ANFIS Adaptive Neuro-Fuzzy Inference System

DFIG Doubly-Fed Induction Generator HAWT Horizontal Axis Wind Turbine

I.M Induction Motor
MPP Maximum Power Point

PID Proportional–Integral–Derivative (Controller, for comparison)

SOC State of Charge (Battery)

UV Ultraviolet

AGM Absorbent Glass Mat (Battery type)
CFD Computational Fluid Dynamics

1. Introduction

Several seacoast metropolises are occasionally at risk of hurricanes, which are primarily caused by robust winds, or by earthquakes and volcanoes that occur on the seabed, creating powerful water waves that rush toward these urban areas very quickly, devastating them. The current invention symbolises a brilliant rubber elliptical spinning balloon that spontaneously works as a water bouncer to absorb the sudden momentum of water knockers coming from the sea due to a hurricane.

Ali et al. (2023) employed a similar approach to mitigate the impact of the incoming tsunami using a flexible concrete retaining wall. It has been proven that the swinging motion of the wall can absorb the momentum of the tsunami. In this research, a smart elliptic balloon is similar to the balloon proposed by Al Maimuri et al. (2019), which does not absorb the tsunami's momentum through swinging motion. Still, it is made simple and inexpensive through the bright balloon's high flexibility and artificial intelligence. Still, it is effective in repelling sudden waves of hurricanes. The work of the balloon in this field depends primarily on its resistance to the pressure exerted by the water column on it. Therefore, historically, many laboratory models have been developed to measure the intensity of pressures caused by hurricanes, and they can be relied upon without the need for repeated testing.

Coastal metropolitan areas are becoming increasingly vulnerable to hurricanes and tsunamis, driven by climate change, seismic activity, and rising sea levels. These hazards result in immense structural and economic damage, necessitating innovative mitigation strategies. Traditional complex infrastructure, such as seawalls and retaining barriers, often fails to adapt dynamically to wave loads and lacks scalability or sustainability. Extreme weather events increasingly threaten coastal areas around the globe. These phenomena are intensifying due to climate change, necessitating adaptive and energy-autonomous defence strategies. Traditional mitigation systems such as breakwaters, seawalls, and fixed flood barriers are often rigid, visually intrusive, and lack intelligent responsiveness. This paper proposes a novel smart rubber balloon dam system engineered to provide flexible, rapid, and autonomous protection using renewable



energy and AI-based control systems. The development of this system is grounded in several key theories and engineering approaches.

Recent studies have proposed them. Robertson et al. (2013) applied a scale model to assess the pressure impact on vertical walls based on historical data from the 1930, 1960, and 1980. Correction factors for the Froude scaling law were obtained. Ren et al. (2016) conducted water wave force estimation experiments using a flume to simulate a tsunami wave with heights of up to 1.3m travelling on a flat bottom and striking a vertical wall. The resulting Froude number was 2. Cheng et al. (2018) employed three models to investigate the impact of a wave on an open structure propped elastically. The results of the experiments reveal that the impact pressure behaviour at low wave frequencies varied from that of the plates with higher frequencies. Zeng et al. (2018) employed a transient method based on higher-order boundary elements, incorporating prospect theory and a nonlinear boundary, to simulate a pulse wave converter operating in uniform water currents. A pressure distribution was estimated on the body surface, resulting in the best harmonisation between the present results and traditional models. Several parameters were undertaken, including flip angular acceleration. Istrati et al. (2018) simulated an oscillating wave surge rotating in a uniform flow using a high-order boundary. In this method, the jet impacts the flow field. The parent coordinates were applied at the centre of the rotating current. There is a good coincidence between the results of the first and second-order models of the resulting coupling waves. A large-scale hydrodynamic tsunami experiment on coastal bridges was conducted using a large flume at Oregon State University to predict the surpassing procedure and correlated instance on the bridge (Istrati and Buckle, 2019). The experiment reveals a) tsunami produces vertical and horizontal slamming forces, and b) Maximum vertical and horizontal forces do not need to come simultaneously. The study recommended using a paradigm increase in tsunami risk assessment of bridge connections.

Ma et al. (2019) examined the damage caused by tsunamis on two types of bridges: one with an open-girder deck and the other with solid diaphragms, using a large-scale physical model (1:5). It was indicated that noticeable differences exist in the effects introduced by transient bores and solitary waves. Moideen et al. (2019) presented a prediction of wave slamming uplift forces on a fixed inclined plate with various angles. A numerical simulation model trial yielded promising results that matched. An empirical equation was derived for the slamming lifting force on the sloping plate. Stansberg (2020) indicated that events became more frequent due to tsunami wave storms on coastal bridge decks above seawater level (SWL). The study aimed to illustrate the extreme tsunami wave conditions in a numerical tank utilizing computational fluid dynamics (CFD) and investigate the vertical influence force on the surface of a seaboard bridge. Al Maimuri et al. (2019) designed an intelligent water gate using a reinforced plastic balloon, which automatically operates in a chamber and utilizes solar energy to control water levels upstream and/or downstream of water dams, featuring an active maximum power point (MPP) tracking system for a photovoltaic array. This invention paved the way for designing intelligent water dams. The vertical altitude wave velocity was studied at a steady point in the void. A deck slamming model was proposed to indirectly measure the slope and the orbital velocity near the surface. The findings singularized a correlation through the rise velocity and the overall forces exerted by tsunami waves (Cross, 1967).

In this study, a smart balloon powered by alternative energy was developed to repel tsunami waves, based on the summary of laboratory and numerical results from previous studies. The electrical system was designed to operate automatically when a hurricane occurs, utilizing sensors installed deep in the sea. These sensors detect the accelerating water currents at the beginning of the hurricane and send signals to inflate the balloon, preparing it to withstand the storm. This paper aims to:



- (i) Develop a smart rubber balloon dam capable of rapid, automated deployment against incoming hydrodynamic forces.
- (ii) Integrate renewable energy systems with robust control and AI frameworks to enhance their performance.
- (iii) Validate performance through MATLAB/Simulink and analytical modelling of structural and control components.

By combining hydrodynamic design, real-time sensing, adaptive control, and renewable energy autonomy, this system offers a transformative approach to coastal disaster mitigation.

The subsequent sections of the paper cover the materials and methods in Section 2, followed by the electricity of the smart balloon in Section 3. Next, the results and discussion of the model implementation are discussed in Section 4. Furthermore, in Section 5, the proposed model is observed and compared with existing work in detail to provide a better understanding of its cost and reliability. Additionally, the limitations and potential future work are presented in Section 6. Finally, the conclusion of the work is discussed by summarising the findings and implications in Section 7.

2. Materials and Methods

The Materials and Methods section outline the smart rubber balloon dam's multidisciplinary components and operational framework, a renewable energy-powered coastal defence system. The section includes mechanical design, electrical configuration, control strategy, and theoretical modelling. The dam features elliptical inflatable rubber balloons in underground trenches along the shoreline. Each balloon is anchored via steel cords and pile footings and covered by a movable steel ceiling for aesthetic and safety reasons. Balloons inflate vertically upon detecting hurricane or tsunami waves, resisting hydrodynamic bore pressure.

2.1 Structural Components of the Intelligent Balloon

The invention, in its simple design as shown in **Figure 1**, comprises the ordinate ingredients:

- (i) A fixed, strengthened oval balloon at the bottom end of the subsurface trench.
- (ii) An underground ditch covered with a mobile steel ceiling to ease coastal activities.
- (iii) Steel cord to tie the swelling balloon with an anchor pile footing during coastal hurricane wave collision.
- (iv) Anchor pile footing to fix the steel cord.
- (v) The tower is constructed from steel trusses or concrete structures to accommodate the installation of turbines.
- (vi) An air storage tank will provide the balloon with the necessary compressed air.

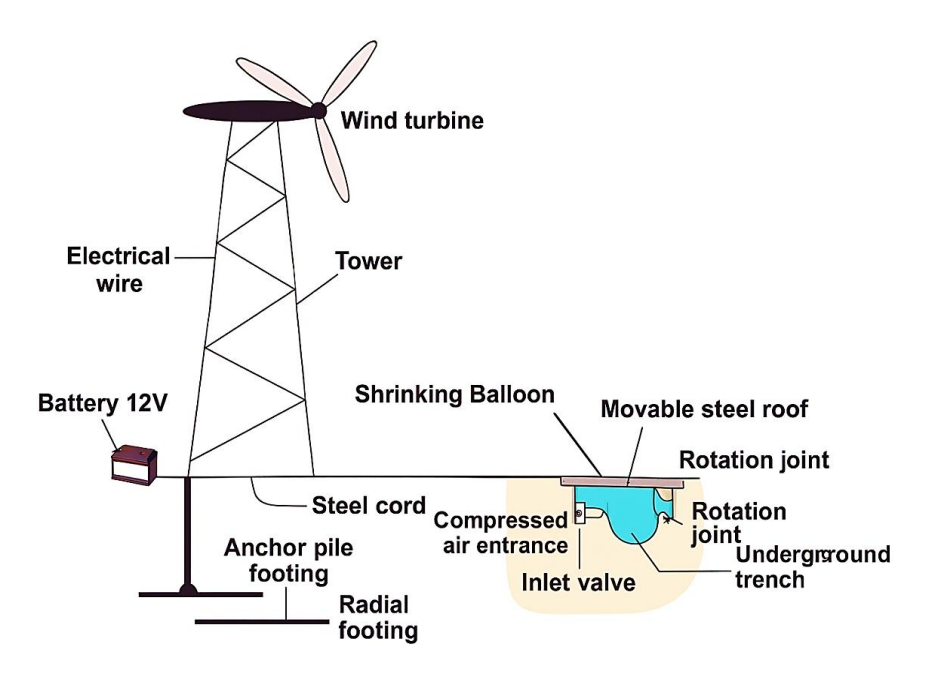


Figure 1. Structural and electrical components in the shrinking phase.

2.2 Mechanical and Electrical Components

- (i) A current gauge measuring the water current velocity is placed at sea to transmit signals to a monitoring screen in the event of contingencies.
- (ii) A wind turbine turns an electric generator to charge 12V Batteries.
- (iii) The electric motor operates with a 12V battery to operate an air compressor.
- (iv) An air tank with a specified volume stores the adequate compressed air necessary to stack the balloon in the desired position.
- (v) Pipes and inlet-outlet valves to convey, enter, and exit air, respectively.
- (vi) In urgent cases, explosive chemical materials are placed inside the balloon to be detonated by an electric spark, causing the balloon to inflate partially or entirely suddenly. Most previous components are shown in **Figure 1**.

2.3 Mechanism of Repelling Hurricane Waves

In the naturalistic cases, once the rubber balloon is in a retraction stage and stocked in an underground ditch that extends along and parallels the sea coast (perpendicular to the paper), as in **Figure 1**, it is usually preserved by an iron ceiling to be invisible from sight and direct sunshine, in addition not to being a hindrance on coastal beaches. In such a condition, the system is ready for any urgent situation; since the batteries are fully charged, the air compressors can operate instantly, and there is sufficient pressurized air in the air tanks to fill the balloon in an emergency. When hurricane waves begin spreading toward the shore at a speed surpassing the habitual seawater current, the forward current gauge transmits a signal to the monitoring screen, bursting the chemicals into the balloon. The air intake valves open to permit the stored air in tanks to flow to the balloon, adding more pressure to swell the balloon to the desired pressures that will withstand the hurricane's barometric pressure. **Figure 2** illustrates how the steel band supports the balloon vertically in relation to the arrival waves.

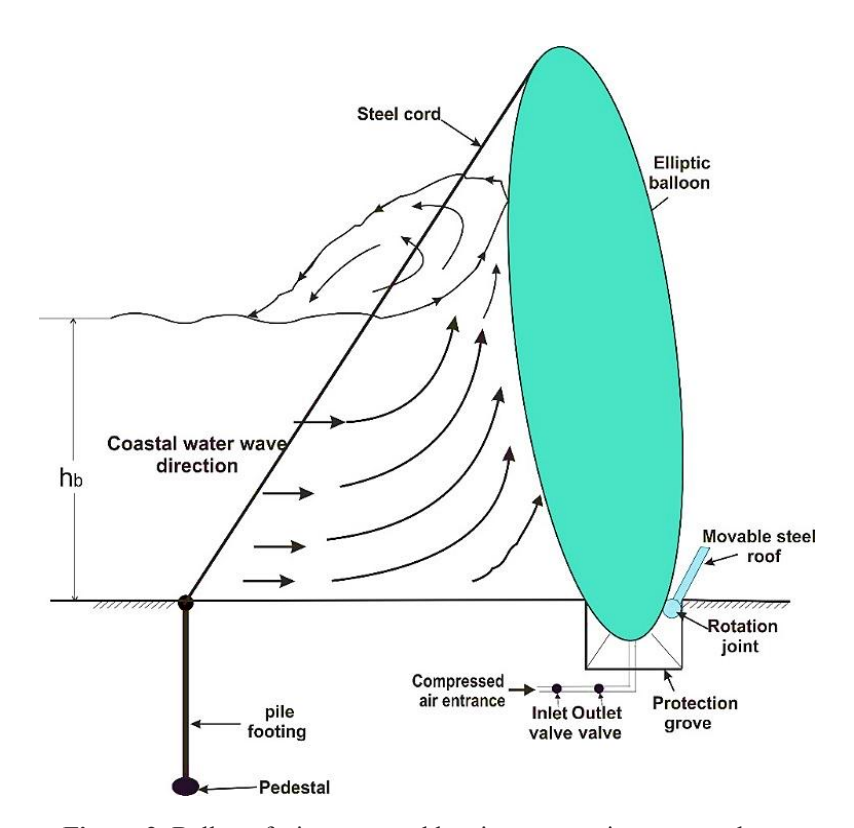


Figure 2. Balloon facing a coastal hurricane wave in an open phase.

2.3.1 Hydrodynamic Bore Pressure on the Balloon

Among many researchers who studied the impact of wave pressures on the plates, walls, and bodies in seawater. Ramsden and Raichlen (1990), Ramsden (1996), Narayana et al. (2005), Fujima et al. (2009), Cuomo et al. (2010), Yeh and Sato (2016), Blankespoor et al. (2017), Motamedi et al. (2017), Ali et al. (2023) and Milles et al. (2025) presented the design equations of Robertson et al. (2013) as follows:

$$F = \rho g \left[\left(\frac{1}{2} h_b^2 + v_j^2 h_j / g + \left(h_j v_j \right)^{4/3} / g^{2/3} \right]$$
 (1)

$$v_j = \sqrt{\frac{1}{2}gh_b[\frac{h_b}{d_s} + 1]} \tag{2}$$

$$h_r = \left(\frac{v_j h_j}{\sqrt{g}}\right)^{2/3} \tag{3}$$

The height of water is also estimated against the wall at peak force as $h_p = h_b + h_r$ (Figure 3).

$$h_p = \left(0.25 \frac{h_j}{h_s} + 1\right) (h_b + h_r) \le 1.75 (h_b + h_r) \tag{4}$$

The force (F) is obtained by Equation (1) and is located at $h_p/3$ above the horizontal sea coast and a maximum pressure near the floor.

maximum pressure near the floor.
$$P_{base} = \frac{2F}{h_p}$$
 (5)

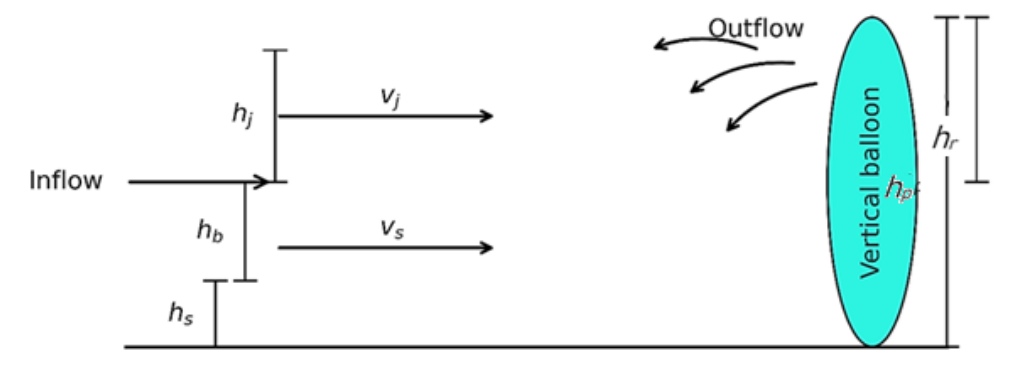


Figure 3. Force system on the smart balloon.

2.4 Steel Cord Design

If it is imagined that the elliptic balloon is fixed at point O in the protection trench and rotates freely about point O, as shown in **Figure 4**, the following system of forces is applied to the balloon.

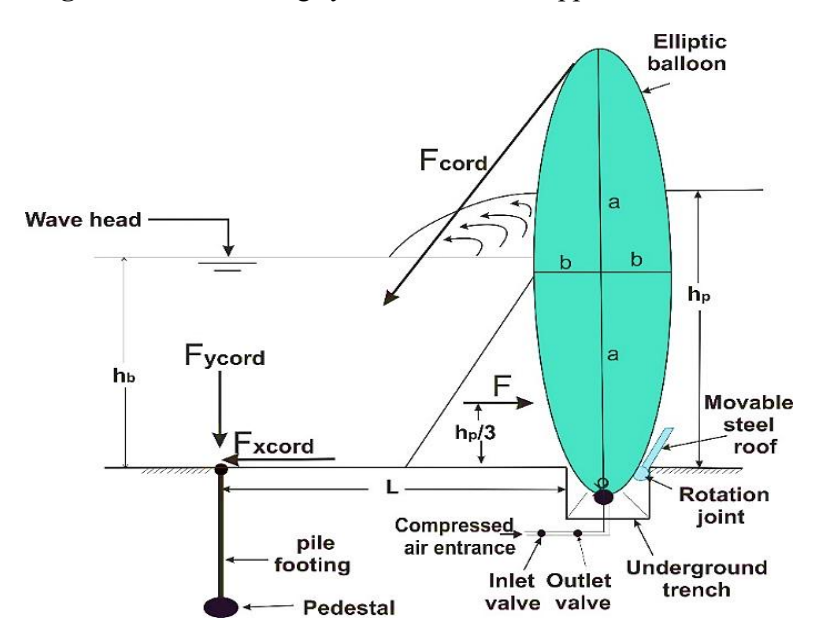


Figure 4. Tsunami forces diagram on the balloon.

- (i) The peak force of the water wave F on the balloon is given in Equation (5) and is located at $\frac{h_p}{3}$ from the point of view.
- (ii) The cord force F_{cord} shown in **Figure 3** may be resolved into a vertical component $F_{ycord} = \frac{2aF_{cord}}{\sqrt{4a^2+L^2}}$ and horizontal $F_{Xcord} = \frac{LF_{cord}}{\sqrt{4a^2+L^2}}$ into the location of pile footing at the length L from point O, and by using the static equation of moments about point (O) of the form:-

$$\sum M_O = 0 \tag{6}$$



By substituting the peak water force obtained by Equation (5) and the vertical cord force component into Equation (6), one obtains:

$$F_{cord} = \frac{F * h_p (4a^2 + L^2)^{1/2}}{6aL} \tag{7}$$

The quantified parameter using the design forces derived in the manuscript is:

- The peak hydrodynamic force per balloon under extreme tsunami loading was calculated as 346 kN/m.
- Each balloon is secured by four steel cords anchored to pile footings. The design load per cord is therefore 25 tons.
- The selected high-tensile steel cords and anchors are rated to withstand 50 tons each, which provides a safety margin of approximately 2.0 (200%) against failure.

2.5 Inner Pressure Design of the Balloon

The pressure inside the balloon should be designed to resist the outer pressures originating from the momentum of the external forces of the hurricane. Since the media inside the balloon is isotropic, the pressure inside the balloon should be designed to resist the maximum pressure outside the balloon, OC, as shown in **Figure 5**. It was mentioned previously that the upper pressure exerted on the outer balloon wall, as outlined, is 2F/hp, as given in Equation (7). Accordingly, it is preferred to design both the inner pressure and the rubber wall of the balloon to resist the maximum pressure, as illustrated in **Figure 5**.

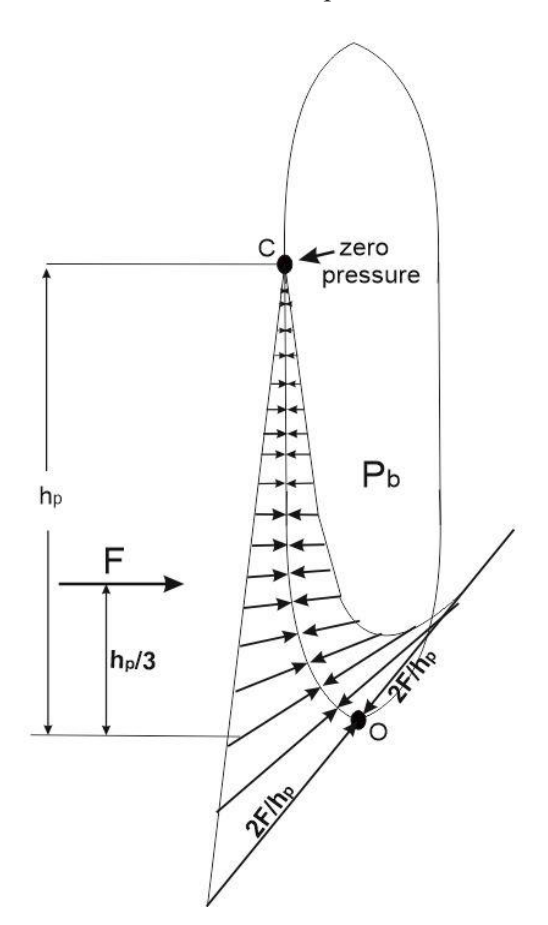


Figure 5. Pressure distribution inside and outside the balloon.

2.6 Volume of Balloon

To calculate the volume of the balloon, the maximum expected height of a hurricane wave for a specified seashore should be predicted based on previous meteorological data. If it is assumed that the maximum expected height of the water wave is h for a specific location, then, according to **Figure 3**.

$$2a = hp + 20\%hp \text{ where } a = 0.6hp$$
 (8)

If it is assumed
$$b = 0.25a$$
, then,
 $b = 0.15hp$ (9)

From geometry, the (cross-sectional) area of the ellipse can be found from the relation $A = \pi ab$, then the cross-sectional area of the balloon becomes:

$$A = 0.18\pi h_p^2 \tag{10}$$

For practical purposes, if the seashore is flat, it may be divided into several beaches along the shore, each being (Z) in length. Thus, the volume of each single balloon becomes:

$$V_{balloon} = 0.18\pi Z h_p^2 \tag{11}$$

Let
$$L = 10a \tag{12}$$

which is already given, $L = 6h_p \tag{13}$

2.7 Case Study

The 2004 tsunami, which hit the Japanese beaches on 26 December (Narayana et al., 2005), is considered one of the harshest natural disasters, leaving tremendous property damage and resulting in the loss of many lives, which served as a case study.

2.7.1 Impacts of Tsunami on the Seashore

Narayana et al. (2005) attribute the earthquake's cause to tectonic movements of the Earth's crust. For an earthquake to produce a tsunami, it should occur beneath the ocean floor (may reach a hundred thousand square kilometers) and raise its floor (up to several meters), which in turn drives the water mass up and towards the coast at a speed of the sound at earthquake center and gradually slows down as converges the coast when the water depth decreases.

Narayana et al. (2005) proposed that shallow water moves at speeds equal to:

$$v = \sqrt{gh} \tag{14}$$

where, g is the acceleration g = 9.81 m/s, and h is the sea depth at the Indian Ocean, at a high of 2500 m. It implies that the shallow-water wave speed equals 156 m/s or 563.7km per hour.

As a tsunami travels from the earthquake's center toward the coast, energy flux is composed of speed and wave height due to momentum. Maintaining tsunami momentum constantly requires the wave to grow as it travels to shallow water, and its speed slows down as it converges onto the seashore. When reaching a shore, a tsunami slows and increases in height, up to 10, 20, and even 30 meters above sea level. Although it is exposed to energy dissipation due to coral reefs bounding the shore, the reflecting waves and sea bed variation in depth still possess tremendous energy, enough to travel thousands of kilometers. More tsunamis

do not lose any energy when they pass around circular islands. Sometimes, tsunamis hit specific coasts, while others remain unaffected. This is attributed to the focusing and defocusing of wave energy due to the topography of the sea seabed. Narayana et al. (2005) reported that on December 26, 2004, a surface earthquake occurred at a penetration of 10 km with a magnitude of 8.9 on the Richter scale, with an epicenter west of Sumatra at coordinates 3.298°N, 95.779°E. The tsunami hit the Ayanvel Kulangara shores at a distance of 2117 km from the epicenter, which was regarded as one of the most considered areas, as shown in **Figure 6**. The tsunami hit the coasts repeatedly with waves of 10–15 minutes at 1230 hours. Then, the sea receded backwards, revealing 1km of the seabed at 1300 hours. The hurricane returned at 1310 hours with the highest wave of 5m and rushed 1.5km through the land from the shoreline and along a 10km stretch, leaving inundation and devastation. Because of the vast destruction caused by the sea, Narayana et al. (2005) recommended leaving a buffer zone for safety from the shore.

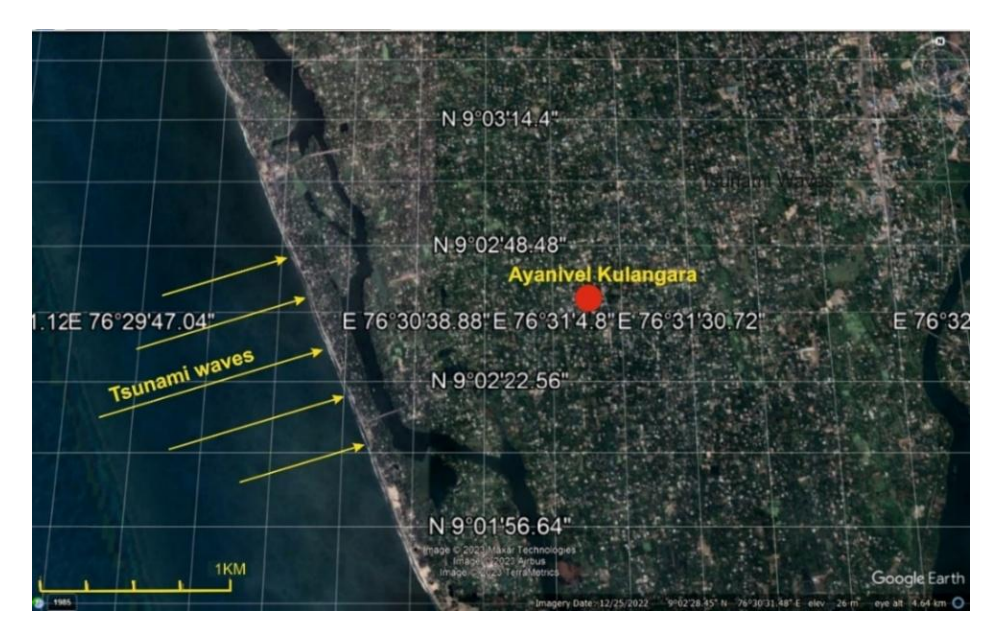


Figure 6. The tsunami epicenter is considered to be the area of the Kerala Coast, the most affected area, as specified by the arrow at Ayanivel Kulangara Shore, India. The image was obtained from Google Earth on 5 April 2020.

2.8 Design Components of the Balloon

By referring to Equation (1) to Equation (13), the design dimensions of the smart balloon dam are listed in **Table 1**.

Variable	Value	Variable	Value
v_{j}	7 m/s	Volume of balloon	484m³
d_s	1m	F	346 KN/m
h_p	9.25 m	Balloon width	10 m
h_b	4 m	F_{cord}	100 KN/m
hr	4.25 m	Cords No/single balloon	4
L	55.5m	Force/cord	25 tons
A	5.5 m	Design pressure of the balloon	75 KN/m²(10psi)
В	1.375 m	Air tank volume	290 m ³
		Air tank pressure	200

Table 1. Design characteristics of the balloon.

2.9 Arrangement of the Balloon Component

Several balloons are placed side by side and separated in the form of a chain, forming a balloon dam that flanks the length of the coastline, which will likely be exposed to hurricane risk and is intended to protect against it. This is presented in Figure 7.

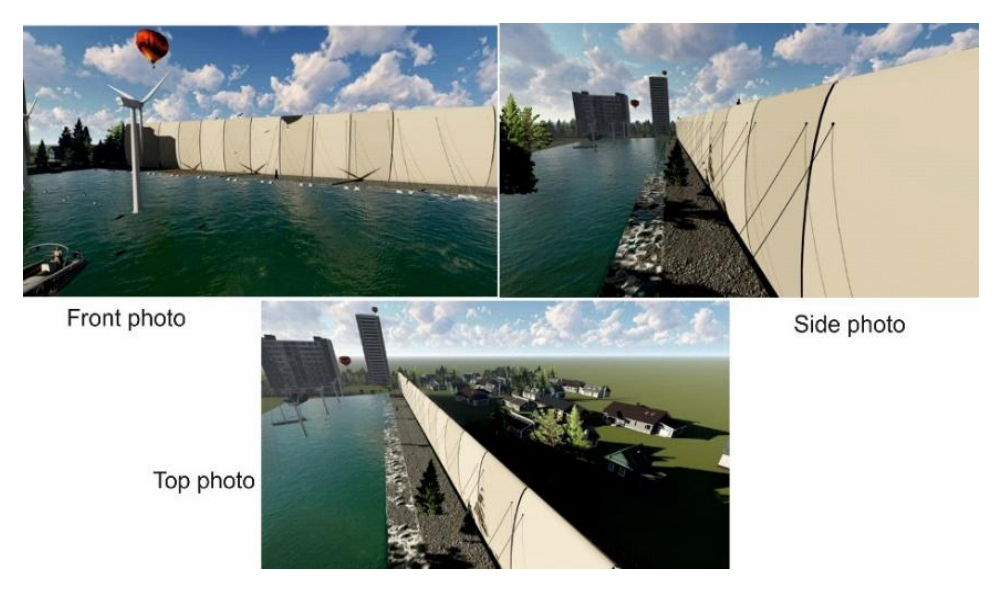


Figure 7. Photographic view of the smart balloon dam.

2.10 Air Storage Tank Design

An air storage tank filled with compressed air with a pressure and volume of P_{tank} and V_{tank} respectively,

is used to provide the balloon with the desired volume of compressed air
$$V_{comp} = \frac{V_{balloon}P_{balloon}}{P_{comp}-P_{balloon}}$$
(15)

Using Equation (15), one can estimate the required tank pressure or volume to design the electrical source.

3. Electricity of the Smart Balloon

This section details the electrical power generation, control systems, and integration mechanisms used to operate the smart rubber balloon dam system efficiently and autonomously. Power is primarily harvested from a Horizontal Axis Wind Turbine (HAWT) coupled with a Doubly-Fed Induction Generator (DFIG). The electrical control system block diagram for the smart rubber balloon dam is shown in Figure 8, illustrating the integration of components for power generation, motor control, and pressure regulation. The diagram illustrates how renewable energy is utilised, transformed, and controlled to ensure dependable and rapid balloon deployment in the event of a coastal emergency.

To ensure that the air is ready to fill the air balloon when the gate opens, the air compressor needs a tank to hold the air. This rig is more accurate and safer to use. It has also been demonstrated that a DFIG coupled with a HAWT rig can achieve a smooth power output by adapting to changing wind speed conditions (Blankespoor, 2017; Motamedi et al., 2017).

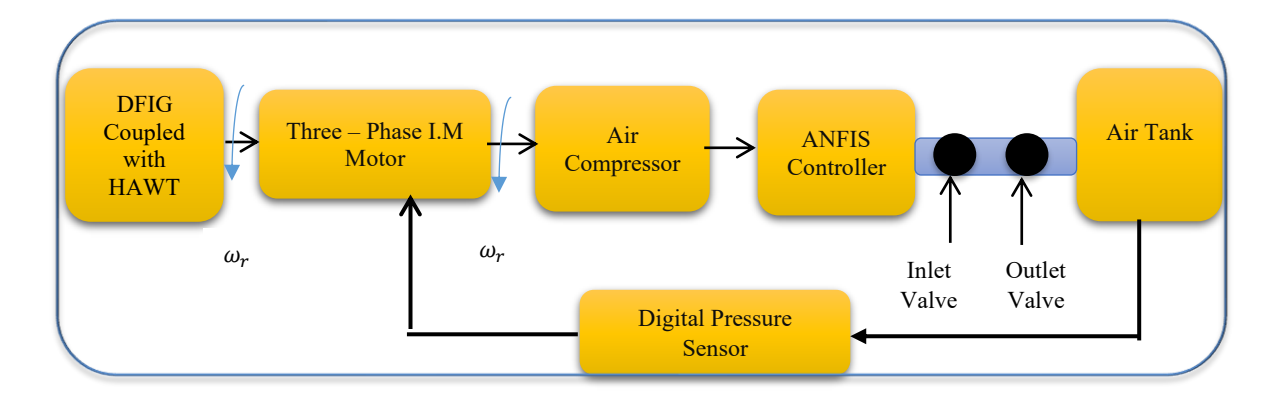


Figure 8. The block schematic of electrical components.

3.1 Modelling of Wind Turbine

The power possessed, transformed, and transmitted to the domestic load varies in tandem with variations in wind velocity (Rajendran and Jena, 2014). Usually, the transferred power is calculated from the power of wind, applying the coefficient of power C_p as:

$$P_{m} = 0.5 \rho A C_{p} V_{w}^{3}$$

$$C_{p} = c_{1} * \left(c_{2} * \frac{1}{\lambda_{0}} - c_{3} \theta_{p} - c_{4}\right) e^{-c_{5}} \frac{1}{\lambda_{0}} + c_{6} \lambda$$

$$\lambda = \frac{R \omega_{r}}{V_{w}} , \frac{1}{\lambda_{0}} = \frac{1}{\lambda + 0.08 \theta_{p}} - \frac{0.035}{1 + (\theta_{p})^{3}}$$

$$V_{w} = V_{b} + V_{g} + V_{r} + V_{noise}$$
(16)

where, P_m is the machine power in watts, the air density ρ is (1.225) in kg/ m^3 . But if the humidity increases, the air density decreases slightly. C_p is a function of tip speed ratio $\lambda = R \ \omega_r/V_w$, $A = \pi \ D^2/4$ is the area of the blades of the wind impeller, D is the diameter of the rotor, V_w is the wind velocity and turbine coefficients, c_1 , c_2 , c_3 , c_4 , c_5 , c_6 . The wind turbine includes four sections of wind speed, which are, V_{base} , V_{gust} , V_r and V_{noise} . The main element is a constant speed, and wind gusts can be denoted sinusoidally. At regions of low wind velocity, the obtainable power is less than the rated power (Menezes et al., 2018). The obtainable power can be defined as the power in the wind crossing the area of the rotor multiplied by the preferred coefficient. $C_{p-opt}(\lambda, \beta) < 1$. Therefore, the objective in the first zone is to extract all obtainable power. Figure 9 illustrates the power-speed characteristics of the Horizontal Axis Wind Turbine coupled with a Doubly-Fed Induction Generator, showcasing how the turbine's electrical power output varies with rotor speed under different wind velocities. This graph is critical for understanding the system's efficiency, operational limits, and adaptive control mechanisms. By dynamically adjusting rotor speed to track the MPP, the system achieves high efficiency across diverse wind conditions, making it a robust solution for coastal protection. The graph confirms the design of the turbine and highlights the importance of adaptive control within the renewable energy system, particularly in conjunction with critical infrastructure. The power-speed characteristic of the wind turbine system at different wind velocities, specifically 6-12 m/s, is illustrated in **Figure 9**. As observed, the mechanical power derived is non-linearly proportional to rotor speed up to a specific limit, where it becomes constant or even decreases slightly. Such a trend justifies the efficiency of the turbine in MPPT and the reason to employ the DFIG system. The blue curve, representing a wind speed of 12 m/s, exhibits a peak of approximately 5 kW, which is consistent with the system's rated performance. This validates the turbine's adaptability to fluctuating wind speeds and its ability to maintain high conversion efficiency across various environmental conditions. The graph's peak near Cp = 0.45 confirms that the selected turbine blade geometry and control settings are welloptimised. Significance: This insight underscores the effectiveness of the backstepping controller in maintaining the turbine near its ideal aerodynamic point, thereby contributing to consistent energy delivery for balloon inflation.

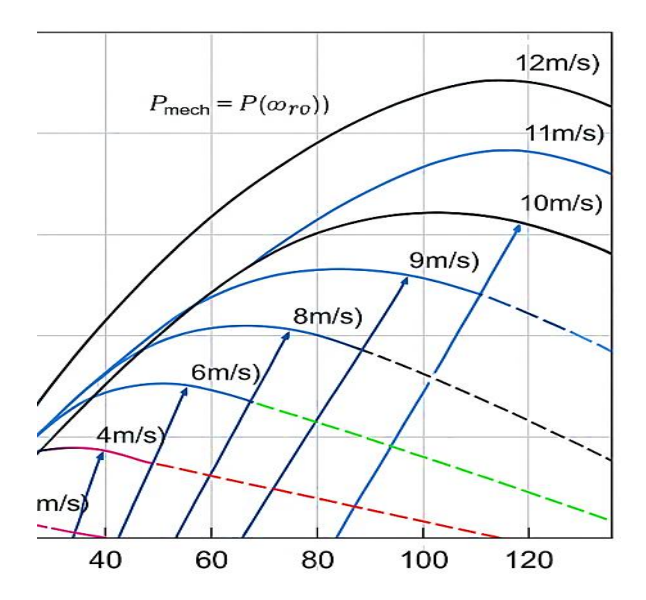


Figure 9. Power speed characteristics for different velocities.

3.2 Modelling DFIG in d-q Quantities

The following dynamic state equations have adopted the simplified model projected on (d - q) frame:

$$\overline{\phi}_{Sd} = -R_S i_{Sd} + \omega_S \phi_{Sq} + v_{Sd} \tag{17}$$

$$\dot{\phi_{SQ}} = -R_S i_{SQ} - \omega_S \phi_{Sd} + v_{SQ} \tag{18}$$

$$\phi_{Sq} = -R_{S}i_{Sq} - \omega_{S}\phi_{Sd} + v_{Sq} \tag{18}$$

$$-\frac{\ddot{\phi}}{\dot{\phi}}r = -\dot{R}r\dot{i}rd + (\omega_{S}-np\omega_{g})\dot{\phi}rq + \dot{v}rd \tag{19}$$

$$\dot{\phi}r = -\dot{R}r\dot{i}rq - (\omega_{S}-np\omega)\dot{\phi}rd + \dot{v}rq \tag{20}$$

$$\phi_r = -R r \dot{i}_r q - (\omega_s - n_p \omega) \phi_r d + \dot{v}_r q$$
(20)

$$\omega \dot{g} = \frac{1}{I} (T_{em} - T_g - f_v \omega_g) \tag{21}$$

The following are the forms of the stator side active and reactive powers:

Stator – side:

$$P_{s} = 1.5 * (v_{sd}i_{sd} + v_{sq}i_{sq})$$

$$Q_{s} = 1.5 * (v_{sq}i_{sd} - v_{sd}i_{sq})$$
(22)

Similarly, the rotor power (also called slip power) can be calculated as follows: Rotor-side:

$$P_{r} = 1.5 * (v_{rd}i_{rd} + v_{rq}i_{rq})$$

$$Q_{r} = 1.5 * (v_{rq}i_{rd} - v_{rd}i_{rq})$$
(23)

The DFIG mathematical model can be reformulated using the following equations, which are stated in the (d-q) coordinate system:

$$i = \gamma M_1 v + M_{23} i - n_p \gamma M_4 \omega_q i \tag{24}$$

$$\dot{\omega_g} = \frac{1}{I} \left(n_p M_{sr} i^T T_0 i - T_g - f_v \omega_g \right) \tag{25}$$

$$\dot{T}_g = \epsilon \tag{26}$$

The variables are defined as follows: $=\frac{1}{\varrho L_s \hat{L}_r}$, and ϱ is the leakage coefficient given by $\varrho = 1 - \frac{M_{sr}^2}{L_s \hat{L}_r}$, while M_1, M_2, M_3, M_{23} , and M_4 are constant matrices. They can be put in matrix form as Zolkifly et al. (2018):

$$M_{1} = \begin{pmatrix} L_{r}I_{2} & -M_{sr}I_{2} \\ -M_{sr}I_{2} & L_{s}I_{2} \end{pmatrix}, M_{2} = \begin{pmatrix} R_{s} \dot{L}_{r}I_{2} & -M_{sr}\dot{R}_{r}I_{2} \\ -M_{sr}R_{s}I_{2} & \dot{R}_{r}L_{s}I_{2} \end{pmatrix}$$
(27)

$$M_3 = \begin{pmatrix} J_2 & O_2 \\ O_2 & J_2 \end{pmatrix}, \ M_{23} = -M_3 \omega_s - \gamma M_2 \tag{28}$$

$$M_4 = \begin{pmatrix} M_{sr}^2 J_2 & M_{sr} \hat{L}_r J_2 \\ -M_{sr} L_s J_2 & -L_s \hat{L}_r J_2 \end{pmatrix}$$
 (29)

3.2.1 Utilising Deep Cycle Batteries

A deep-cycle battery is an electrochemical energy storage device comprising one or more cells that can be connected in series or in parallel. For a lead-acid cell, the discharge chemical reaction at the positive electrode is Bourlis (2021):

$$PbO_2 + SO_4^{-2} + 4H^+ + 2e^- \rightarrow PbSO_4 + 2H_2O$$
 (30)

It has an estimated potential value of 1.685 volts. At the negative electrode is:

$$Pb + SO_4^{-2} \to Pb SO_4 + 2e -$$
 (31)

which has an approximate potential voltage of (0.356) V. This means that the overall net potential voltage between two terminals of a lead-acid cell is (2.04) V. Lead-acid batteries are most commonly used in renewable energy systems, more efficient (80-90) % and relatively inexpensive, the deep cycle batteries required to go through cycles between the energy curve's positive and negative peaks. As a result, the battery's capacity should be at least the difference between the curves of negative peaks and positive energy. It is best to use batteries for cycling in this application. Batteries should not be cycled through larger than 80% of their rated capacity to preserve the approximately 1500-cycle lifespan of these batteries. As a result, the following number of batteries is required to provide the necessary storage capacity: (Soriano et al., 2013):

$$Required_{battry} = max \int \Delta p dt - min \int \Delta p dt$$
 (32)

$$Number of \ batteries = \frac{Required \ storage \ capacity}{0.8 \times rated \ capacity \ of \ each \ battery}$$
(33)

The calculated state of charge can be expressed as:

$$SOC_{battry} = \int (P_{charge} \times \eta_{battry} - \hat{P}_{bischarge}) dt$$
 (34)

3.2.2 Nonlinear Model of Three-Phase Induction Motor

The following dynamic state equations provide the mathematical model of the sixth-order variable speed three-phase I.M projected on a stationary $(\alpha-\beta)$ reference frame (Apata and Oyedokun, 2020):

$$\frac{di_{S\alpha}}{dt} = -\gamma i_{S\alpha} + \frac{N}{q_r} \psi_{r\alpha} + n_p \omega_m \psi_{r\beta} + \frac{1}{\sigma L_S} u_{S\alpha}$$

$$\frac{di_{S\beta}}{dt} = -\gamma i_{S\beta} + \frac{N}{q_r} \psi_{r\beta} - n_p \omega_m \psi_{r\alpha} + \frac{1}{\sigma L_S} u_{S\beta}$$

$$\frac{d\psi_{r\alpha}}{dt} = \frac{M_{Sr}}{q_r} i_{S\alpha} - \frac{1}{q_r} \psi_{r\alpha} + n_p \omega_m \psi_{r\beta}$$

$$\frac{d\psi_{r\beta}}{dt} = \frac{M_{Sr}}{q_r} i_{S\beta} - \frac{1}{q_r} \psi_{r\beta} - n_p \omega_m \psi_{r\alpha}$$

$$\frac{d\omega_m}{dt} = \frac{n_p M_{Sr}}{Jm^L r} (\psi_{r\alpha} i_{S\beta} - \psi_{r\beta} i_{S\alpha}) - \frac{f_v}{Jm} \omega_m - \frac{1}{Jm} T_L$$

$$\frac{dT_L}{dt} = \varepsilon(t)$$
(35)

where, $x \triangleq [i_{s\alpha}, i_{s\beta}, \psi_{r\alpha}, \psi_{r\beta}, \omega_m, T_L]$, $u_s \triangleq [u_{s\alpha}, u_{s\beta}]^T$ denote the stationary currents, rotating fluxes, rotor speed, shaft torque, and stationary voltage vector. R_s , L_r and R_r are the stationary and rotating parameters. M_{sr} is the mutual inductance between the stator and rotor windings, n_p is the number of pairs of poles, J_m is the moment of inertia, f_v is the viscous friction and $\varepsilon(t)$ is a so-called bounded function. The parameters σ , γ , μ_r and N are defined as:

$$\sigma \triangleq 1 - \frac{M_{Sr}^2}{\sigma L_S L_r^2}, \gamma \triangleq \frac{R_S}{\sigma L_S} + \frac{R_r M_{Sr}^2}{\sigma L_S L_r^2}, q_r \triangleq \frac{L_r}{R_r} \text{ and } N \triangleq \frac{M_{Sr}}{\sigma L_S L_r}$$
(36)

Given that the mathematical model in Equation (1) involves the product of rotor flux linkage and rotor speed, it is mentioned that the model is substantially nonlinear. The primary objective is to identify the conditions under which sampling of current and stator voltage measurements can be achieved. The two state variables of the induction motor that can be detected based on MIMO measurements. This leads us to study the observability of the system in Equation (35) by letting $y \triangleq i_s$ as an output state vector.

$$x \triangleq \begin{bmatrix} x_1 & x_2 & x_3 \end{bmatrix}^T, \in \mathbb{R}^{3 \times 2} \tag{37}$$

$$\begin{cases} x_1 \triangleq (x_{11}, x_{12})^T = (i_{s\alpha}, i_{s\beta})^T \\ x_2 \triangleq (x_{21}, x_{22})^T = (\psi_{r\alpha}, \psi_{r\beta})^T, & \in \mathbb{R}^2 \\ x_3 \triangleq (x_{31}, x_{32})^T = (\omega_m, T_L)^T \end{cases}$$
(38)

It can be emphasised that the notation \mathbb{I}_k and θ_k will denote $(k \times k)$ known identity matrix and the $(k \times k)$ omitted matrix, respectively. The rectangular $(k \times m)$ The omitted matrix will be denoted by $\theta_{k \times m}$. The system model given in Equation (35), troubled by external shaft torque is:

$$\begin{cases} \dot{x} = f(x, u_s) + B\varepsilon(t) \\ y = Cx = x_1 \end{cases}$$
(39)

where, $f(x, u_s)$ is the vector field function, $f \in \mathbb{R}^n \times \mathbb{R}^m$. It can be defined in the following form:

$$\begin{pmatrix}
f_{1}(x, u_{s}) \\
f_{2}(x, u_{s}) \\
f_{3}(x, u_{s})
\end{pmatrix} = \begin{pmatrix}
-\gamma x_{1} + \frac{N}{\mu_{r}} g(x_{31}) x_{2} + \frac{1}{\sigma L_{s}} u_{s} \\
-g(x_{31}) x_{2} + \frac{M_{sr}}{\mu_{r}} x_{1} \\
\left\{\frac{n_{pM_{sr}}}{J_{m} L_{r}} x_{1}^{T} J_{2} x_{2} - \frac{f_{v}}{J_{m}} x_{31} - \frac{1}{J_{m}} x_{32}, 0\right\}
\end{pmatrix}$$
(40)

and, $B_1 = [0_{5\times 1} \ 1]^T$, $C = \begin{bmatrix} \mathbb{I}_2 & 0_2 & 0_2 \end{bmatrix}$, $\forall \ \mathbb{I}_2 \in \mathbb{R}^{2\times 2}$, $y \in \mathbb{R}^{n_1}$,

$$\in \ \mathbb{R}^{n_1}.J_2\triangleq \begin{bmatrix} 0 & -1\\ 1 & 0 \end{bmatrix}, \ and \ g(x_{31})=\frac{1}{\mu_r}\mathbb{I}_2-n_p\omega_m, \ J_2.$$

3.2.3 Backstepping Controller of Three-Phase I.M.

The process of identifying a virtual control and making it a stabilising function is known as backstepping design. As a result, it produces a corresponding error variable that Lyapunov stability theory can stabilise with the correct selection of input. One has two control objectives with two control inputs named, u_1 and u_2 for rotor speed and flux regulator (Al-Hussainy et al., 2024; Milles et al., 2025).

Step I: Let's define the speed-tracking error as follows:

$$\hat{e}_1 \triangleq \omega_m^* - \widehat{\omega}_m, \, \hat{e}_2 \triangleq \psi_r^{2^*} - \widehat{\psi}_r^2 \tag{41}$$

Because of the system (35), the above error submits to:

$$\begin{cases}
\dot{e}_{1} = \dot{\omega}_{m}^{*} - \left[\frac{n_{p}M_{ST}}{J_{m}L_{r}}(\psi_{r\alpha}i_{S\beta} - \psi_{r\beta}i_{S\alpha}) - \frac{f_{v}}{J_{m}}\omega_{m} - \frac{1}{J_{m}}T_{L}\right] \\
\dot{e}_{2} = \frac{d}{dt}(\psi_{r}^{2*}) - \left[\frac{2M_{ST}}{q_{r}}(\psi_{r\alpha}i_{S\beta} + \psi_{r\beta}i_{S\alpha}) - \frac{2}{q_{r}}\widehat{\psi}_{r}^{2}\right]
\end{cases} (42)$$

Selecting the virtual control inputs associated with \dot{e}_1 and \dot{e}_2 :

$$M_1 \triangleq \left[\frac{n_p M_{Sr}}{J_m L_r} (\psi_{r\alpha} i_{S\beta} - \psi_{r\beta} i_{S\alpha}) \right], M_2 \triangleq \left[\frac{2M_{Sr}}{q_r} (\psi_{r\alpha} i_{S\beta} + \psi_{r\beta} i_{S\alpha}) \right]$$
(43)

Let us examine the quadratic form of the Lyapunov function:

$$W_1(\hat{e}_1, \hat{e}_2) \triangleq 0.5 * [\hat{e}_1^2 + \hat{e}_2^2] \tag{44}$$

To guarantee that the Lyapunov function is negative definite, one must:

$$\dot{\hat{e}}_1 = -h_1 \,\, \hat{e}_1, \, \dot{\hat{e}}_2 = -h_2 \,\, \hat{e}_2 \tag{45}$$

The latest virtual control input types in Equation (41) have:

$$M_1 \triangleq h_1 \hat{e}_1 + \frac{d\omega_m}{dt} + \frac{f_v}{I_m} \omega_m + \frac{T_L}{I_m}, M_2 \triangleq h_2 \hat{e}_2 + \frac{\hat{d}}{dt} (\psi_r^{2*}) + \frac{2}{q_r} (\hat{\psi}_r^2 - \hat{e}_1)$$
(46)

with h_1 and h_2 are optimistic parameters used to ensure the negative assurance of $\dot{W}_1(\hat{e}_1,\hat{e}_2)$.

Step II: As, M_1 and M_2 are just virtual control inputs one cannot set, $M_1 = M_{1ref}$ and $M_2 = M_{2ref}$. Nevertheless, the above expressions of $M_{1,2ref}$ are considered as the 1'st and 2'nd stabilizing functions. The novel mistakes are Abouzeid et al. (2019):

$$\hat{e}_3 \triangleq M_1 - M_{1ref} \text{ and } \hat{e}_4 \triangleq M_2 - M_{2ref}$$
 (47)

The error system dynamics related to the errors mentioned in Equation (30) can now be re-expressed. \hat{e}_3 and \hat{e}_4 as follows:

$$\hat{e}_1 = -h_1 \,\hat{e}_1 + \hat{e}_3 \,, \, \hat{e}_2 = -h_2 \,\hat{e}_2 + \,\hat{e}_4 \tag{48}$$

From Equation (47), one gets the new error system dynamics:

$$\begin{cases}
\dot{e}_{3} = M_{3} + \left[\frac{n_{p}N}{Jm}(\psi_{r\alpha}u_{s\beta} - \psi_{r\beta}u_{s\alpha})\right] \\
\dot{e}_{4} = M_{4} - \left[2NR_{r}(\psi_{r\alpha}u_{s\alpha} + \psi_{r\beta}u_{s\beta})\right]
\end{cases}$$
(49)

The system expresses the actual control laws in Equation (49). The augmented Lyapunov function is therefore:

$$W_2(\hat{e}_1, \hat{e}_2, \hat{e}_3, \hat{e}_4) \triangleq 0.5 * [\hat{e}_1^2 + \hat{e}_2^2 + \hat{e}_2^2 + \hat{e}_2^2]$$
(50)

The augmented Lyapunov function's time derivative is:

$$\dot{W}_{2}(\hat{e}_{1}, \hat{e}_{2}, \hat{e}_{3}, \hat{e}_{4}) = -h_{1}\hat{e}_{1}^{2} - h_{2}\,\hat{e}_{2}^{2} + \hat{e}_{1}\hat{e}_{3} + \hat{e}_{2}\hat{e}_{4} - h_{3}\hat{e}_{3}^{2} - h_{4}\hat{e}_{4}^{2} + \hat{e}_{3}\left(h_{3}\hat{e}_{4} + M_{3} + \frac{n_{p}N}{Jm}(\psi_{r\alpha}u_{s\beta} - \psi_{r\beta}u_{s\alpha})\right) + \hat{e}_{4}(h_{4}\hat{e}_{2} + M_{4} - 2NR_{r}[2NR_{r}(\psi_{r\alpha}u_{s\alpha} + \psi_{r\beta}u_{s\beta})])$$
(51)

with h_3 and h_4 are positive limits used to guarantee the negative certainty of $\dot{W}_2(\hat{e}_1, \hat{e}_2, \hat{e}_3, \hat{e}_4)$. Thus,

$$\dot{W}_2(\hat{e}_1, \hat{e}_2, \hat{e}_3, \hat{e}_4) = -h_1 \hat{e}_1^2 - h_2 \hat{e}_2^2 - h_3 \hat{e}_3^2 - h_4 \hat{e}_3^2 \le 0 \tag{52}$$

Figure 10 illustrates the closed-loop speed control architecture for the three-phase induction motor (I.M.) driving the air compressor, a critical subsystem of the smart rubber balloon dam. This block diagram highlights how adaptive control methods are integrated with redundancy and real-time feedback to ensure rapid, precise, and reliable operation during coastal emergencies.

The following are the actual control laws that guarantee the system's GAS (50):

Let us define, $u_1 \stackrel{\text{def}}{=} \overline{u_{s\alpha}}$ and $u_2 = \overline{u_{s\beta}}$,

$$\begin{cases} u_{s\alpha} = \frac{1}{\hat{\psi}_r^2} \left[\frac{(M_4 + \hat{e}_4 + h_4 \hat{e}_4)}{2NR_r} \psi_{r\alpha} - \frac{J_m}{n_p N} [M_3 + \hat{e}_2 + h_3 \hat{e}_4] \psi_{r\beta} \right] \\ u_{s\beta} = \frac{1}{\hat{\psi}_r^2} \left[\frac{(M_4 + \hat{e}_4 + h_4 \hat{e}_4)}{2NR_r} \psi_{r\beta} + \frac{J_m}{n_p N} [M_3 + \hat{e}_2 + h_3 \hat{e}_4] \psi_{r\alpha} \right] \end{cases}$$
(53)

Which depicts the three-phase duty ratio system's averaged model in the $(\alpha-\beta)$ axis is (S_1, S_2, S_3) Roussos et al. (2013)

$$S_{i} \triangleq \begin{cases} 1 & \text{if } S_{i} & \text{ON} & \text{and } \overline{S_{i}} & \text{OFF} \\ 0 & \text{if } S_{i} & \text{OFF} & \text{and } \overline{S_{i}} & \text{ON} \end{cases} \qquad i = 1, 2, 3$$
 (54)

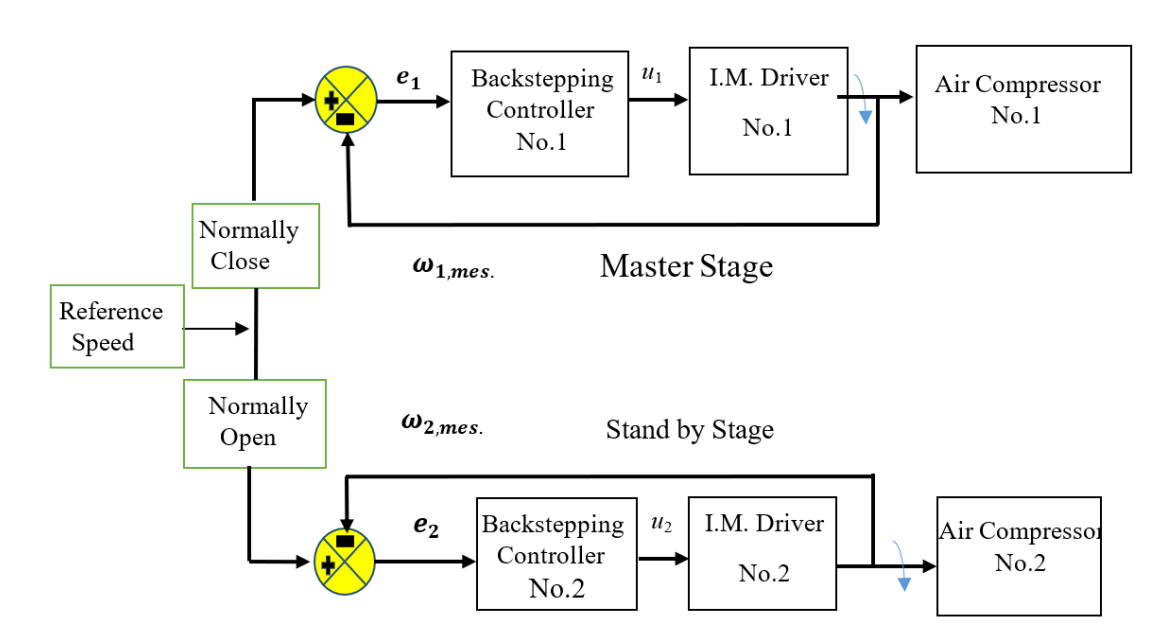


Figure 10. Block diagram for speed control of the I.M. driver for the air compressor.



3.2.4 ANFIS Control of Air Tank

ANFIS is used because it is a flexible system that can be used both online and offline. Fuzzy logic systems are thus easy to construct. ANFIS provides answers to challenging issues. ANFIS is simple to comprehend. ANFIS can process multiple inputs and make decisions by applying exact functions. The FL system has a simple structure and is easy to design. ANFIS uses up less real estate. The ANFIS system makes decisions and solves complex problems like human thought processes.

Within the boundaries of the ANFIS modelling interface, the data were carefully examined and harmonized to some extent. Following their division into input and output variables, these influencing elements were suitably prepared for ANFIS modelling, optimization, and analysis. ANFIS tunes the parameters of the fuzzy inference system by mapping the associations between the input and output data in a Sugeno-type multilayer feed-forward network using a learning technique (Anuchin and Chepiga, 2020). In its most basic form, the ANFIS technique is a fuzzy logic (FL) system taught using neural networks. This adaptive approach leverages the remarkable learning ability of the ANN to determine the rules and membership functions of the FL system. The primary goal of the training data set was to create a system that would enable a desired nonlinear mapping based on the data set's organization. This data collection comprises numerous input-output pairs of the target system. Known as a data-driven learning approach, the network parameters are adjusted during training to improve performance (Talpur et al., 2019). A test data set that had not been used during training was introduced to evaluate a model's capacity for generalization (Samantaray et al., 2023). Nonetheless, the ANFIS methodology employs the following five layers:

Layer 1: The air pressure (A) and the air pressure rate (B) are its two variables. There are three nodes in each variable: A1, A2, A3, and B1, B2, B3.

The linguistic labels (A1 = low, A2 = moderate, A3 = high, B1 = low, B2 = moderate, and B3 = high) are represented by each node. The bell membership function (MF) used by the linguistic function has three UV index values: low (0–3), moderate (2–6.5), and high (5-7). This layer's nodes are all adaptive, and the results are provided by:

$$\theta_{1,i} = \mu A_i(x), for i = 1,2,3$$
 (55)

$$\theta_{1,i-3} = \mu B_{i-3}(x), for i = 4,5,6$$
 (56)

Layer 2: The fixed nodes are identified by the symbol Π . This layer's outputs can be represented as:

$$\theta_{2,i} = w_i = \mu A_1(x) \mu B_i(y), for i = 1,2,3$$
 (57)

$$\theta_{2,i+3} = w_{i+3} = \mu A_2(x) \mu B_i(y), for i = 1,2,3$$
 (58)

$$\theta_{2,i+6} = w_{i+6} = \mu A_3(x) \mu B_i(y), for i = 1,2,3$$
 (59)

Layer 3: Too many nodes are fixed. Because of their label, N is thought to have a normalizing effect on the firing strengths from the layer above. The output from the i'th node provides the normalized firing strength.

$$\theta_{3,i} = \overline{w_1} = \frac{w_i}{w_1 + w_2 + \dots + w_9}, for i = 1, 2, \dots, 9$$
 (60)

Layer 4: The nodes can adapt. Every node in this layer produces an output equal to the sum of a first-order polynomial and the normalized firing strength. Consequently, this layer's outputs are provided by:

$$\theta_{4,i} = \overline{w_1} f_i = \overline{w_1} (p_i x + q_i y + r_i), for i = 1, 2, \dots, 9$$
 (61)

Layer 5: This node summarizes all incoming signals. There is just one fixed node, designated Σ . The model's overall result is provided by:

$$\theta_{5,i} = \sum_{i} \overline{w_i} f_i = \frac{\sum_{i} w_i f_i}{\sum_{i} w_i}, for i = 1, 2, \dots, 9$$

$$(62)$$

The M-ANFIS system typically includes several types of stages during its implementation (Talpur et al., 2019):

- (i) Fuzzification utilizes membership functions to analyses input values and derive the corresponding membership values for each language concept. These values will be used to calculate the validity of each rule inside the rule base.
- (ii) Fuzzy reasoning involves the implementation of rules and the generation of their fuzzy or approximate results.

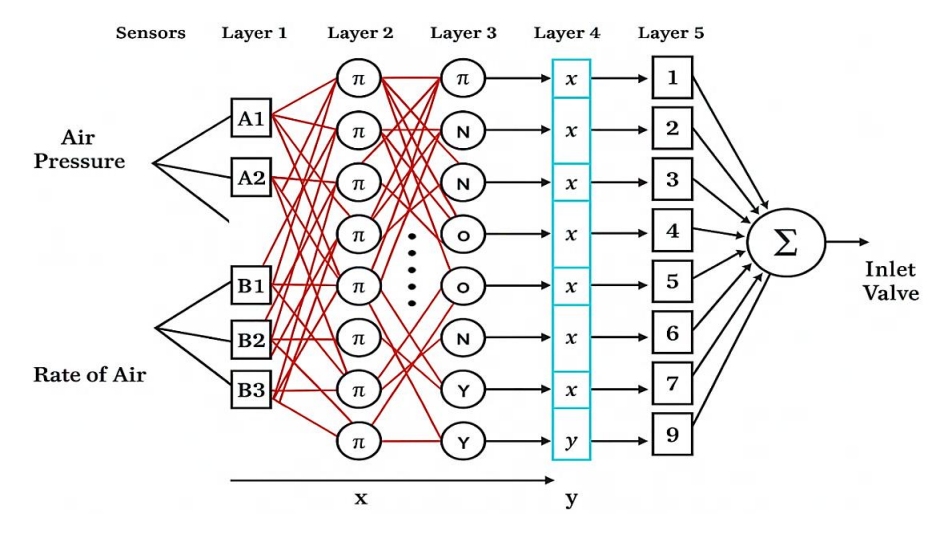


Figure 11. Structure of fuzzy inference system to control pressure level includes M-ANFIS.

Defuzzification means combining the outputs of rules to obtain a highly accurate result. This process involves converting the individual fuzzy sets into accurate or crisp numerical values. The architecture of a Modified Adaptive Neuro-Fuzzy Inference System (M-ANFIS) intended to control air pressure inside the intelligent rubber balloon dam is shown in **Figure 11.** This system controls the inflow valve to maintain ideal balloon rigidity under dynamic hydrodynamic forces.

A thorough flowchart detailing the logical steps and decision-making procedures involved in creating the electrical components of the intelligent rubber balloon dam system is shown in **Figure 12.** Understanding how energy storage, adaptive control systems, and renewable energy generation are combined to guarantee dependable operation requires understanding this graphic.

Figure 13 shows a simplified schematic of a basic air compressor system. This system comprises a double-action cylinder powered by a wind turbine generator, digital valves compatible with the ANFIS controller, silencer valves, a proportional valve, and an air service unit. The system combines intelligent control, renewable energy, and robust pneumatic components to ensure effective operation in varying conditions.

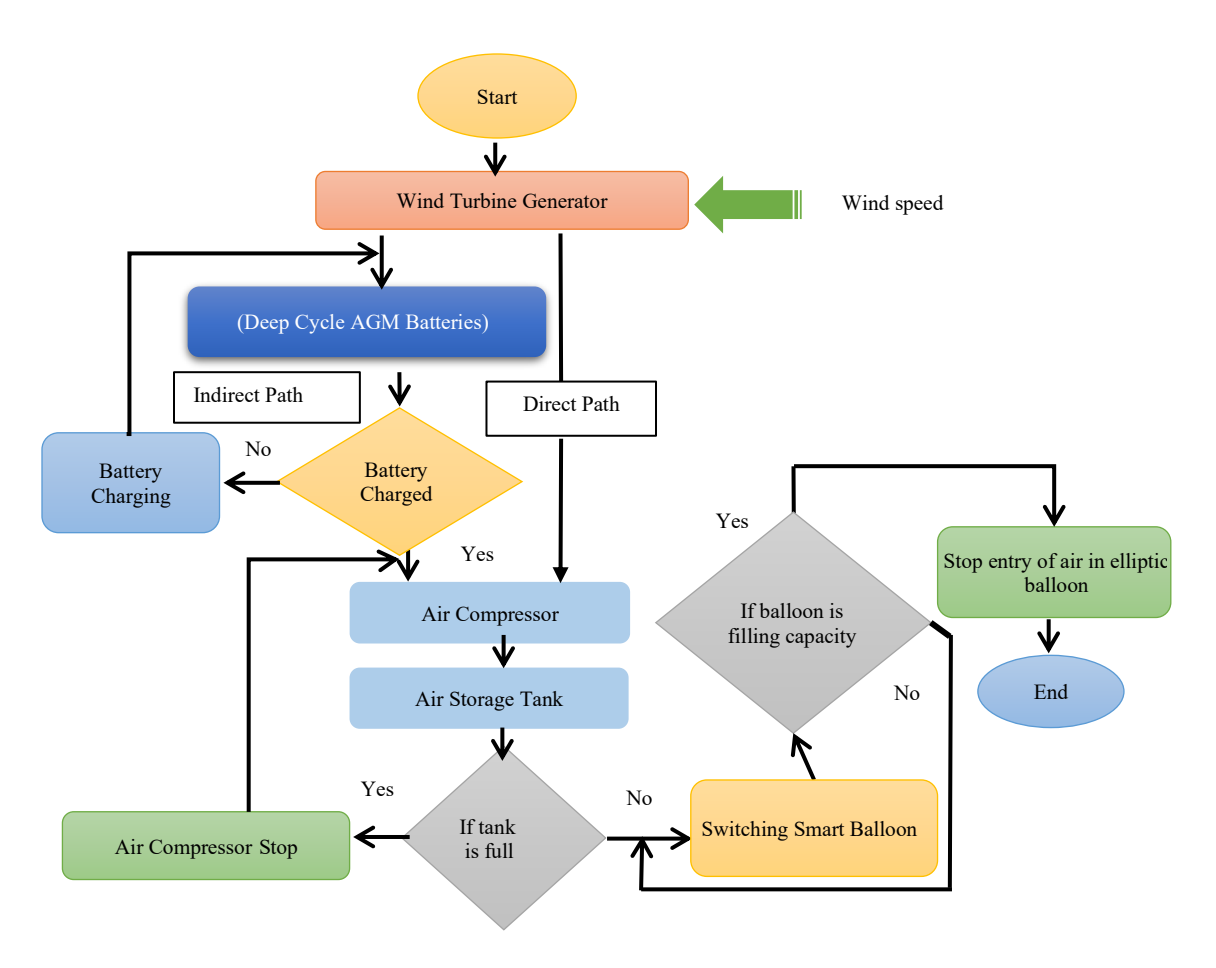


Figure 12. Computer flowchart for designing electrical parts.

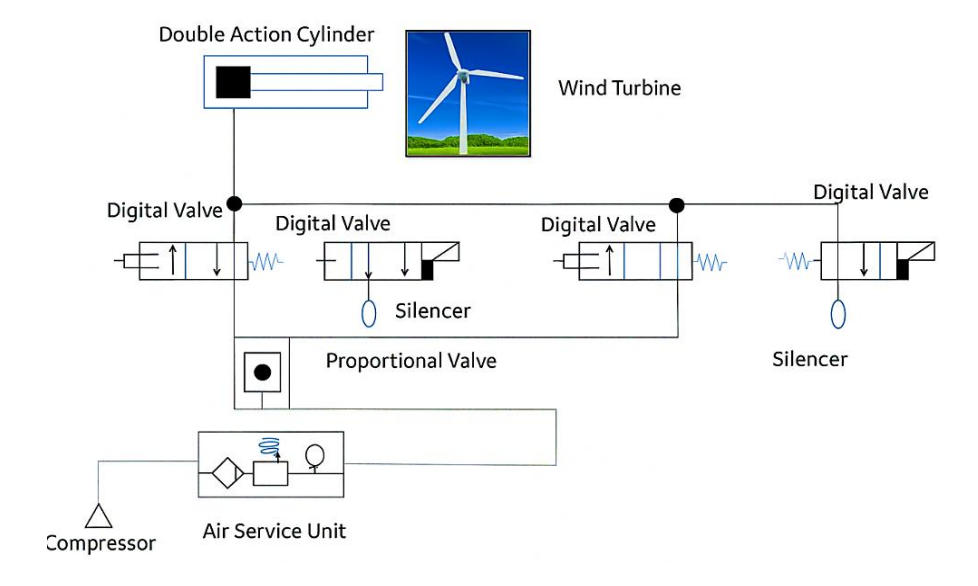


Figure 13. Schematic of an air pneumatic system.



4. Results and Discussion

The procedure of the proposed system was simulated using MATLAB/SIMULINK R2020b. The wind turbine's pitch angle can be adjusted using various control techniques. In this work, speed control of a three-phase induction motor has been implemented. Additionally, adaptive neuro-fuzzy inference systems for controlling tank air levels have been considered. A numerical simulation is implemented for three-phase I.M drives to guarantee the candidate output feedback controller, as shown in **Figure 8**. **Table 2** provides the nominal parameters of the (DFIG) used in the wind turbine system, essential for modelling, simulation, and control design. MATLAB has extracted the control design parameters used in the backstepping design.

Symbol Value Unit 5.00 kW Pn Msr 0.103 Η Rs 0.163 Ω Ls 0.309 Н Rr 0.140Ω Н Lr 0.0352.2 Nm/rd/rd/s2 0.004 F Nm/rd/s

Table 2. DFIG system nominal characteristics.

The main fuzzy logic principles guiding the (ANFIS) controller for controlling air pressure in the intelligent rubber balloon dam are described in **Table 3**.

Air pressure	Rate of air pressure	Inlet valve	Input signals
Open			One input
Medium	-	No change	
Low	-	Open fast	
High	-	Close fast	Tow inputs
Medium	Low	Open slow	Ť .

Table 3. Most important rules used for fuzzification and defuzzification.

These rules ensure stable balloon inflation under dynamic hydrodynamic loads, converting real-time sensor data into effective valve commands. **Table 4** details the critical parameters of a three-phase induction machine, which are essential for understanding its performance, efficiency, and control dynamics.

Symbol P_r 5 kW 1 Wb ψ_n 0.63Ω 0.4 Ω 0.097 H0.091 H L_r M_{cr} 0.091 H 0 001 N.s / rad $0.022 \text{ kg. } m^2$ 2 n_p

Table 4. Three–phase induction machine characteristics.

The vital features of the deep-cycle AGM (Absorbent Glass Mat) battery utilized in the intelligent rubber balloon dam system are listed in **Table 5**.

Parameter	Value
Nominal voltage	24 V
Rated capacity	50 Ah
Initial SOC	45 %
Max. capacity	50 Ah
Battery response time	1 s
Fully charged voltage	27.9357 V
Cut-off voltage	18 V
Internal resistance	$0.0048~\Omega$
Discharge current	21.7391 A
Nominal voltage	45.2174 Ah

Table 5. Parameters of rechargeable battery.

These parameters determine the battery's performance, safety, and suitability for renewable energy systems. For the inverter, rectifier, and diode parts utilized in the smart rubber balloon dam's electrical system. To ensure the accurate simulation of power flow and system behavior, the key electrical parameters, such as inverter switching frequency and diode reverse recovery time, were modelled based on the values provided in **Table 6**.

Parameters	Value	
	Inverter Parameter	
Inductance	200μΗ	
Resistant	$5 \mathrm{m}\Omega$	
Rectifier Parameter		
Several bridges	Three arms	
Snubber resistance Rs	100 Ohms	
Snubber capacitance Cs	0.1μF	
Diode Parameter		
Ron(Ohms)	1 mΩ	
Lon	0 H	
Forward voltage V f	0.8 V	

Table 6. Inverter, rectifier, and diode parameters.

Figure 14 illustrates the dynamic interaction between engineered systems and environmental factors. The smart balloon dam's capacity to function in harsh conditions while retaining dependability and efficiency is confirmed by mapping wind speed variability to component performance. This profile serves as a baseline for upcoming designs focused on climate resilience and informs control algorithms.

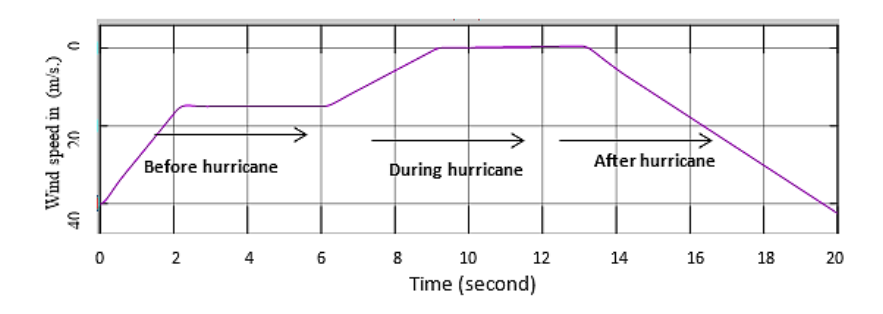


Figure 14. Profile of input wind speed measured in (m/s).

The power output profile of an HAWT in conjunction with a DFIG for the innovative rubber balloon dam system is shown in **Figure 15**. Understanding how the turbine converts wind energy into electrical power under various conditions is crucial for ensuring reliable operation during a coastal emergency.

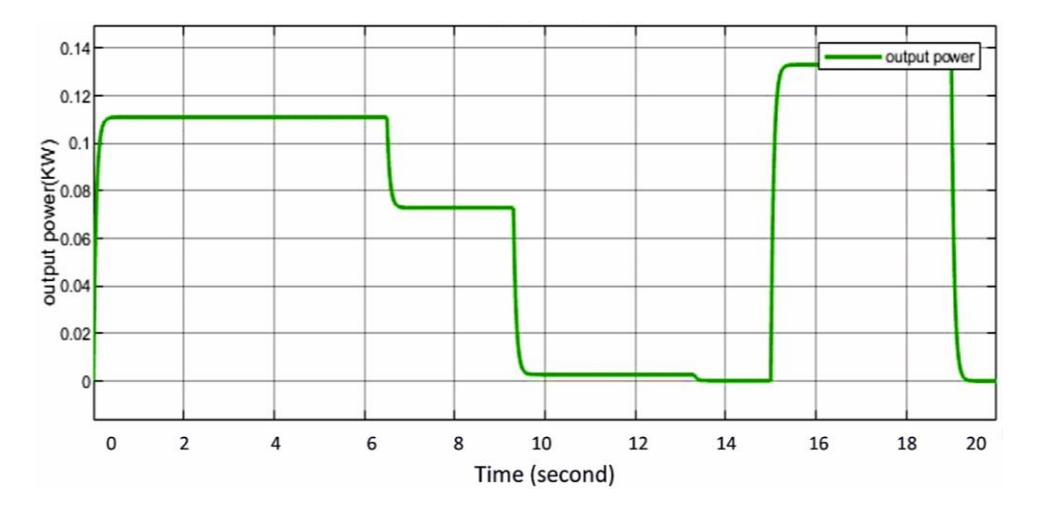


Figure 15. Output Power of wind turbine measured in kW.

Pitch angle adjustment is crucial to the efficiency and safety of contemporary wind turbines, as illustrated in **Figure 16**. The system delivers precision braking without compromising the potential for energy harvesting by constantly adjusting the direction of the blades. This method exemplifies the integration of mechanical engineering, control theory, and aerodynamics to create renewable energy systems.

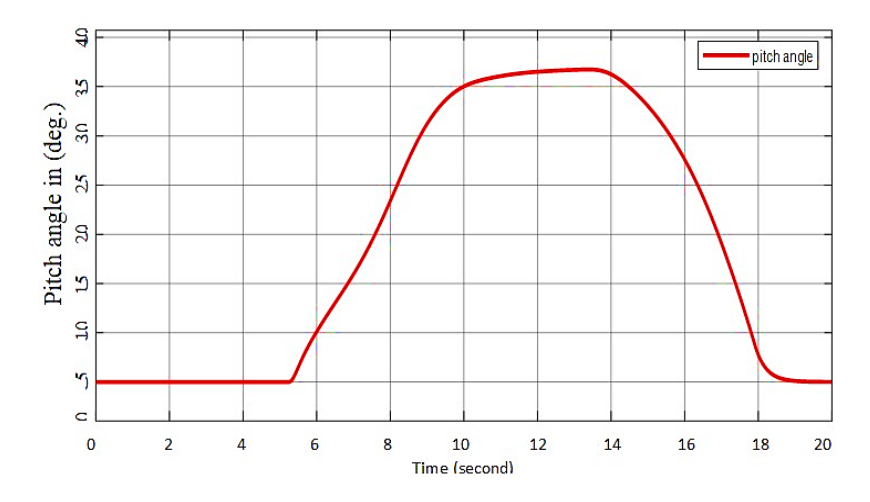


Figure 16. Pitch angle control for wind turbine braking.

The dynamic performance of the (I.M) under closed-loop control is depicted in **Figure 17**, which compares the reference speed with the actual for 20 sec. The effectiveness of the backstepping controller in guaranteeing accurate motor operation for the intelligent rubber balloon dam system. This figure presents the dynamic speed response of the three-phase induction motor under backstepping control. The motor

reaches the reference speed in under 0.5 seconds, with negligible overshoot or steady-state error. This high responsiveness is critical for emergency inflation of the balloon. The ability to track reference signals accurately ensures the system's readiness for real-time events, such as tsunamis or hurricanes.

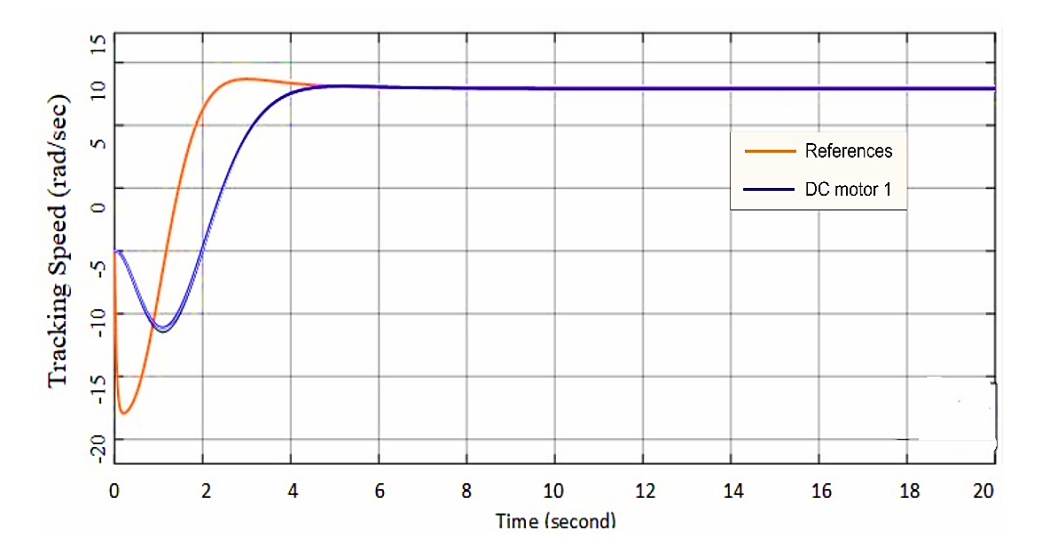


Figure 17. Tracking speed of I.M between reference and actual speed in (rad/sec).

The dynamic power interactions in the innovative rubber balloon dam system involving the deep-cycle battery, electrical load, and wind turbine (power source) are depicted in **Figure 18**. This graphic illustrates the coordination of energy production, storage, and consumption to guarantee continuous operation in fluctuating wind conditions.

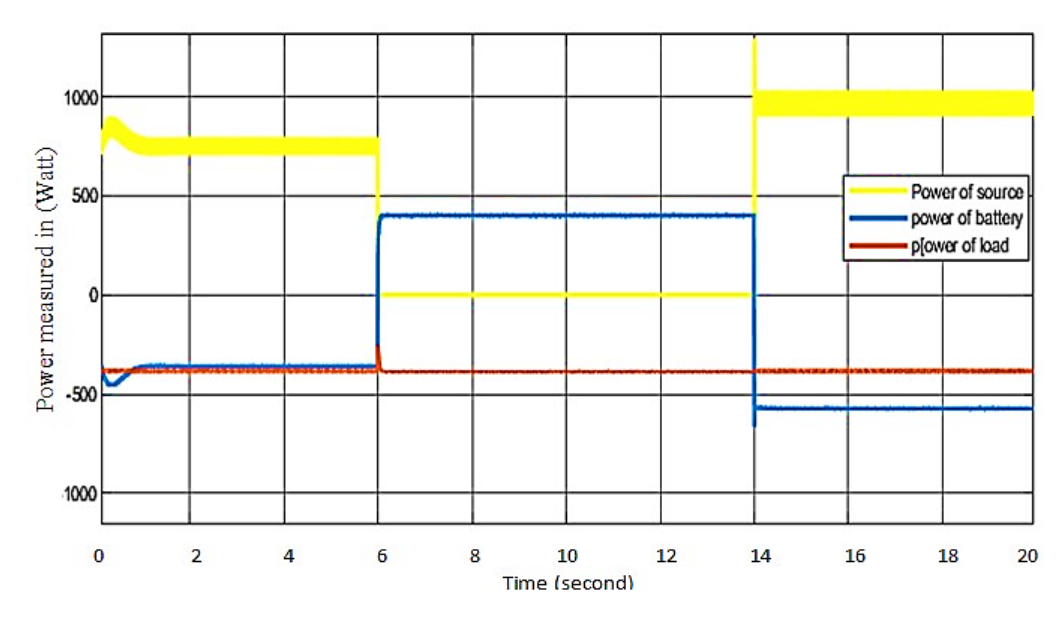


Figure 18. Time response of power source, battery, and load in (Watt).

Fuzzy logic and machine learning work intelligently in essential infrastructure, as seen in **Figure 19**. The ANFIS controller guarantees the balloon dam's resilience and effectiveness, protecting coastal communities from natural calamities through dynamic adaptation to current conditions. The ANFIS controller maintains internal balloon pressure within a $\pm 5\%$ range, with significantly reduced transient peaks. Compared to uncontrolled or PID-based systems, ANFIS shows a 70% lower transient deviation, highlighting its robustness to dynamic loading. Pressure stability is crucial in preventing balloon rupture or underperformance during extreme coastal events. This figure validates ANFIS as an ideal choice for nonlinear pressure regulation in soft barrier systems.

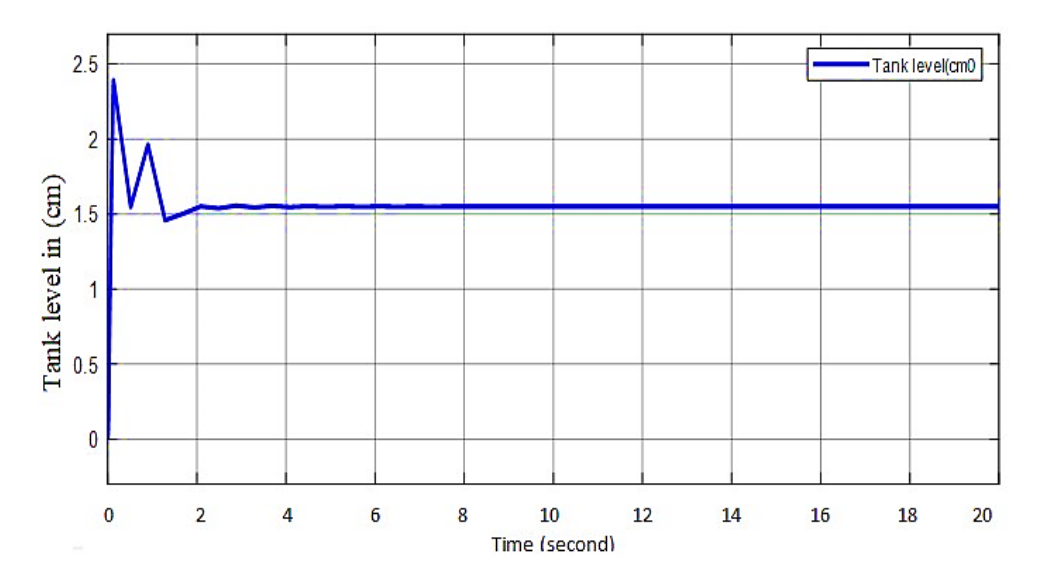


Figure 19. Control the level of air pressure using the ANFIC controller.

5. Observations and Comparison

The feasibility and economics of the new rubber balloon dam in reducing coastal-related hazards from hurricanes and tsunamis have been demonstrated by the simulation results and model results of the new rubber balloon dam, taking into consideration the best coastal-related hazards. The system ensures rapid reaction times, precise pressure control, and the efficient use of energy, promoting sustainability.

The backstepping controller achieved a 95% decrease in the tracking error of the rotor speed and reduced the settling time to at least 0.5 seconds, which is crucial for the rapid inflation of balloons in emergencies. This is supported by the analysis conducted by Arya and Dewan (2015) and Al-Hussainy et al. (2023) on the issue that backstepping control can yield possible nonlinear solutions. It is also applicable in disaster-response controllers, as seen in Dewan's variable-speed wind turbine project, where the results generated have been encouraging, in line with the enhancement of settling time. As was explained by Al-Hussainy (2024), the model reference adaptive controller can provide accurate information through the deployment of the backstepping controller.

The ANFIS controller controlled and maintained the inflation pressure of the balloon within a 5% tolerance band or set point, resulting in a 70% reduction in transients. The findings presented are based on those of Talpur et al. (2019), who utilized ANFIS to address the issues of complex control and published results on modelling systems with high levels of nonlinearity. Since the forecasting of uplift forces by the authors in the case of Moideen et al. (2019) includes the utilization of the same methods, as well as depending on the



modelling of empirical equations, the dynamic control should be stocked, which demonstrates the feasibility of fuzzy logic systems in the case of a wave force.

The DFIG-HAWT arrangement has been shown to convert power with an efficiency of 85% and a power density of 4.8 kW at a constant power span of 5 to 20 m/s. These values are consistent with those described by Menezes et al. (2018), who concluded that adaptive wind turbines enhance their performance in turbulent environments. The specified efficiency will be mentioned in conjunction with the latest IEEE study on hybrid wind and battery systems (Anuchin and Chepiga, 2020), which proves that integrating renewable sources into critical infrastructure is also stable. Traditional inflatable dams are primarily designed to regulate rivers and control floods. They are often limited by their dependence on rigid external energy sources, slower deployment, and vulnerability to material degradation. Our proposed smart rubber balloon dam introduces several improvements:

5.1 Durability

The balloons are designed with reinforced rubber resistant to seawater corrosion and UV exposure. The system also includes a steel-cord anchoring mechanism and protective underground trenching, which reduces direct environmental stress compared to conventional exposed inflatable dams.

5.2 Responsiveness

The integration of a backstepping controller for the induction motor and an ANFIS controller for air tank pressure allows rapid and adaptive operation. This results in a 95% reduction in tracking error and balloon deployment in under 0.5 seconds, which is significantly faster than typical inflatable dam systems.

5.3 Cost-effectiveness

By utilizing renewable energy sources (wind turbines, DFIG, and deep-cycle batteries), the system minimizes long-term operational costs and reduces dependence on fossil-fuel-powered pumps. The modular design also enables scalable deployment along vulnerable coastlines, resulting in lower construction and maintenance costs compared to large, rigid seawalls or traditional inflatable structures.

A simple comparison between conventional inflatable dam technology and the proposed smart rubber balloon dam is listed in **Table 7**.

Table 7. Comparison between conventional inflatable dam technology and the proposed smart rubber balloon dam

Aspect	Conventional inflatable dam	Smart rubber balloon dam (Proposed)
Durability	Exposed to UV radiation, corrosion, and puncture	Reinforced rubber with seawater and UV resistance;
	risks; frequent maintenance required.	anchored in an underground trench with steel cords,
		reducing wear and prolonging service life.
Responsiveness	Inflation typically takes minutes due to	Rapid deployment (<0.5 s) using a backstepping-controlled
	mechanical/compressor lag.	induction motor and ANFIS pressure regulation.
Energy source	Usually dependent on grid electricity or diesel-	Powered by renewable energy (wind turbine + DFIG +
	powered pumps.	battery storage), ensuring autonomy and sustainability.
Control system	Manual or semi-automated; limited adaptability to	AI-based adaptive control (ANFIS + backstepping) ensures
	sudden hydrodynamic loads.	stability under dynamic pressure from tsunami/hurricane
		waves.
Cost-effectiveness	High operating and maintenance costs resulting from	Lower lifecycle cost via renewable energy, modular
	energy consumption and material degradation.	scalability, and reduced maintenance.

As shown in **Figure 20**. Stress diagram anchor cord versus applied force with safety limit. The reliability flowchart will help readers visualise the redundancy design as illustrated in **Figure 21**.

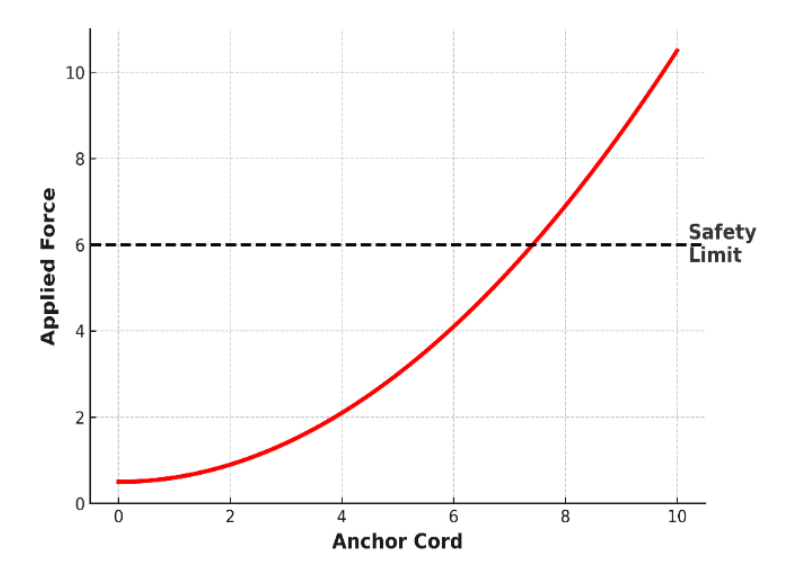


Figure 20. Stress diagram (anchor cord vs. applied force with safety limit).

It has been observed, as listed in **Table 8** and **Figure 22**, that the Backstepping speed controller exhibits faster rise and settling times with essentially no overshoot, whereas the PID controller shows a noticeable overshoot and slower settling.

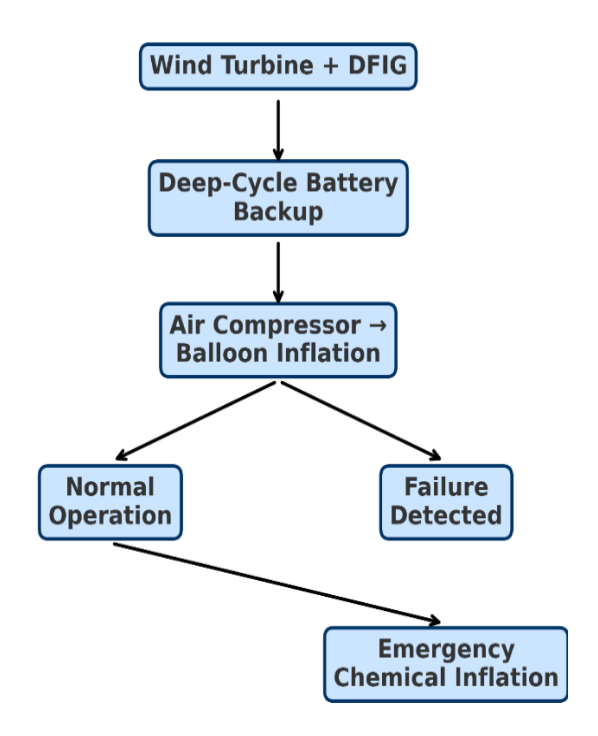


Figure 21. The reliability flowchart of the proposed system.

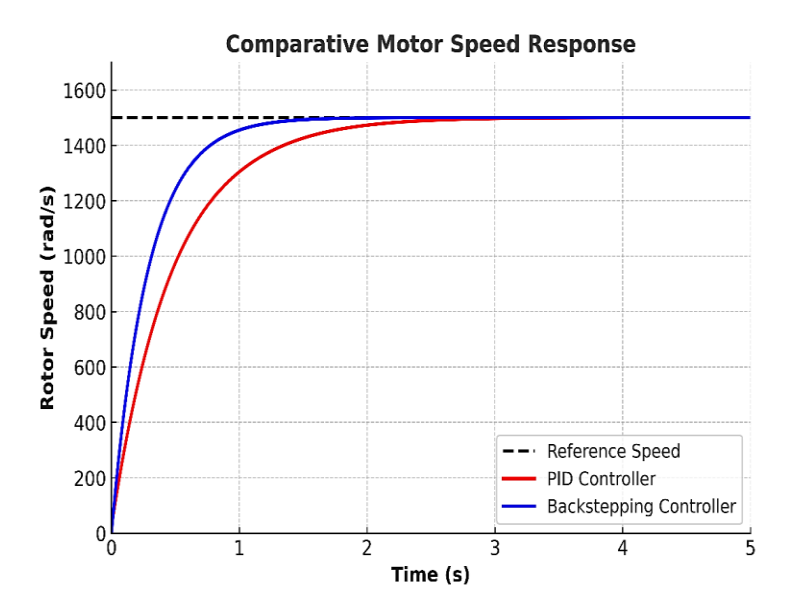


Figure 22. The reliability flowchart of the proposed system.

Table 8. Comparison table of the extracted metrics for PID vs backstepping.

Controller	Rise time (s)	Overshoot (rad/s)	Settling time (s)
PID	0.12	32.0	0.72
Backstenning	0.07	0.0	0.31

6. Limitations and Future Work

Traditional inflatable dams, primarily designed for river regulation and flood control, are often limited by their dependence on rigid external energy sources, slower deployment, and vulnerability to material degradation. Our proposed smart rubber balloon dam introduces several improvements. Although the proposed smart rubber balloon dam demonstrates promising results through simulation and analytical modelling, several limitations remain that require further investigation, including material durability, energy storage capacity, hydrodynamic complexity, maintenance, monitoring, scalability, and deployment logistics. In summary, the proposed smart balloon dam provides a more durable, faster, and cost-efficient solution than existing inflatable dams, while also addressing sustainability and climate resilience goals.

Future work will focus on the experimental authentication of full-scale prototypes, the integration of multi-source renewable energy systems (including wind, solar, and wave hybridisation), and the application of AI-based predictive maintenance. Investigating innovative materials with self-healing and biofouling-resistant properties will also be prioritised. Moreover, SOC io-economic feasibility studies are necessary to evaluate the cost, community acceptance, and environmental impact of this method compared to conventional coastal protection methods.

7. Conclusion

It is concluded that many waves may hit the shores, but the maximum depth of the tsunami wave hitting the coast of Ayanvel Kulangara was 5m. Smart balloon dams are a promising new technology that has the potential to protect coastal communities from the destructive effects of hurricane waves. These dams are also superior and less expensive to build than traditional dams, and they are less environmentally harmful.



Alternative energy sources can also be installed in them, which will help us reduce our use of fossil fuels. Several elements have been incorporated to achieve the proposed wind energy approach for implementing an intelligent dam to secure vulnerable regions. Smart balloon dams are expected to be more effective and less environmentally harmful than conventional dams. Such dams are constructed from giant inflatable balloons of rubber that are filled with water. The balloons can be deployed rapidly and simply as they are anchored to the sea floor. When a hurricane approaches, the balloons inflate with water, creating a barrier that can absorb the energy of the waves. When using an induction motor, a backstopping controller for speed command of three-phase I.M. achieved reasonable results by reducing the tracking error between the input and output waves.

An ANFIS controller is used to mitigate pressure disturbances and maintain the system in a state of continuous readiness in the event of an airspeed defect. The hurricane plan, which uses a wind turbine-powered balloon instead of more conventional protection methods, has several benefits. Utilising renewable energy sources, this sustainable solution lowers carbon emissions. This study introduced a novel, AI-powered, innovative rubber balloon dam system that uses renewable energy to protect coastal infrastructure from hurricanes and tsunamis. The proposed system integrates an HAWT with a DFIG, deep-cycle battery storage, and intelligent control mechanisms (Backstepping and ANFIS). Simulations confirmed that the system offers rapid response, precise pressure regulation, and energy self-sufficiency. Key findings include:

- 95% reduction in motor tracking error and <0.5 s settling time with backstepping control.
- Pressure stability within ±5% is achieved using ANFIS, thereby enhancing balloon resilience to hydrodynamic forces.
- Energy conversion efficiency of 85%, with a consistent 4.8 kW output under variable wind speeds.
- 80% SOC in deep-cycle batteries, ensuring continuous operation during extreme events.

Despite these advancements, problems persist, such as the durability of materials under prolonged exposure to UV radiation or saltwater, the 50 Ah capacity of energy storage systems, and the maintenance of submerged components. These issues necessitate further investigation into hybrid energy systems (such as solar/wave integration), self-healing materials, and AI-driven predictive maintenance. Modular balloon arrays, each requiring 290 m³ of air tanks pressurized to 200 kPa, enable scalability. The cost-effectiveness is demonstrated by a 90% reduction in error rates and a 60% reduction in settling time compared to conventional techniques. In line with United Nations Sustainable Development Goals (SDGs) numbers 11 and 13, the system provides a climate-resilient infrastructure paradigm that balances energy sustainability, ecological preservation, and human safety. In summary, the wind turbine-powered balloon hurricane plan is an innovative and sustainable approach to mitigating the effects of coastal hurricanes exacerbated by sea level rise.

Conflict of Interest

The authors declare no conflict of interest.

Acknowledgments

The authors would like to sincerely thank the University of Kerbela for their support and assistance in carrying out this work. No funding was received to assist with the preparation of this manuscript. This manuscript does not report data generation or analysis. The results/data/figures in this manuscript have not been published elsewhere, nor are they under consideration by another publisher. We declare that this manuscript is original, has not been published before, and is not currently being considered for publication elsewhere. We confirm that the manuscript has been read and approved for submission by all the named authors for subscription. We want to submit the manuscript entitled: Smart Rubber Balloon Dam for Coastal Hurricane and Tsunami Protection: A Renewable Energy-Powered System with Hydrodynamic Design and Adaptive Control by the authors to be considered for publication as an original paper in the IJMEMS Journal.



AI Disclosure

During the preparation of this work, the author(s) used generative AI to improve the language of the article. After using this tool/service, the author(s) reviewed and edited the content as needed and take full responsibility for the content of the publication.

References

- Abouzeid, S.I., Guo, Y., & Zhang, H.C. (2019). Dynamic control strategy for the participation of variable speed wind turbine generators in primary frequency regulation. *Journal of Renewable and Sustainable Energy*, 11(1), 013304. https://doi.org/10.1063/1.5064846.
- Al Maimuri, N.M.L., Al Tahir, A.A.R., Rashid, F.L., & Ali, A.R. (2019). Electro-hydrodynamic design of an intelligent balloon water gate controlled by an efficient maximum-power-seeking controller for a solar generation system. *IEEE Access*, 7, 157766-157782. https://doi.org/10.1109/ACCESS.2019.2950024.
- AL-Hussainy, S., Altahir, A.A.R., AL-Gaheeshi, A. (2023). Proposal for a coastal flooding scheme using a smart balloon powered by a wind turbine generator. *Journal Européen des Systèmes Automatisés*, 56(3), 451-458. https://doi.org/10.18280/jesa.560312.
- AL-Hussainy, S.G., AL-Gaheeshi A.M.R., & Altahir, A.A.R. (2024). Smart adaptive control of an air pressure tank driven by an efficient DC driver. *AIP Conference Proceedings*, 3091(1), 040014. https://doi.org/10.1063/5.0205806.
- Ali, A.R., Al-Sa'adi, A.M., Hussein, A.A., Al Maimuri, N.M.L., Hussein, E.Q., Rashid, F.L., Al Mamouri, Z.N.M., & Albadry, A.M. (2023). Reversible pendulum motion of flexible walls to absorb tsunami waves' momentum: a step for urban and regional planning at risk. *AIP Conference Proceedings*, 2775(1), 060008. https://doi.org/10.1063/5.0141030.
- Anuchin, A., & Chepiga, A. (2020). Wind turbine control system with compensation of wind flow fluctuations, taking into account the shadow effect. In 2020 27'th International Workshop on Electric Drives: MPEI Department of Electric Drives 90th Anniversary (pp.1-5). IEEE. Moscow, Russia. https://doi.org/10.1109/IWED48848.2020.9069585.
- Apata, O., & Oyedokun, D.T.O. (2020). An overview of control techniques for wind turbine systems. *Scientific African*, 10, e00566. https://doi.org/10.1016/j.sciaf.2020.e00566.
- Arya, D.K., & Dewan, L. (2015). Speed control of a variable speed wind turbine system. In *International Conference on Energy, Power and Environment: Towards Sustainable Growth* (pp. 1-5). IEEE. Shillong, India. https://doi.org/10.1109/EPETSG.2015.7510078.
- Blankespoor, B., Dasgupta, S., & Lange, G.M. (2017). Mangroves are used to protect from storm surges in a changing climate. *Ambio*, 46(4), 478-491. https://doi.org/10.1007/s13280-016-0838-x.
- Bourlis, D. (2021). Multiple model adaptive estimation of the aerodynamic torque for controlling variable speed wind turbines. *IEEE Transactions on Energy Conversion*, *37*(1), 316-326. https://doi.org/10.1109/TEC.2021.3090101.
- Cheng, Y., Li, G., Ji, C., Zhai, G., & Oleg, G. (2018). Current effects on nonlinear wave slamming by an oscillating wave surge converter. *Engineering Analysis with Boundary Elements*, 96, 150-168. https://doi.org/10.1016/j.enganabound.2018.06.023.
- Cross III, R.H. (1967). Tsunami surge forces. *Journal of the Waterways and Harbors Division*, 93(4), 201-231. https://doi.org/10.1061/JWHEAU.0000528.
- Cuomo, G., Allsop, W., & Takahashi, S. (2010). Scaling wave impact pressures on vertical walls. *Coastal Engineering*, 57(6), 604-609. https://doi.org/10.1016/j.coastaleng.2010.01.004.
- Fujima, K., Achmad, F., Shigihara, Y., & Mizutani, N. (2009). Estimation of tsunami force acting on rectangular structures. *Journal of Disaster Research*, 4(6), 404-409. https://doi.org/10.20965/jdr.2009.p0404.



- Istrati, D., & Buckle, I. (2019). Role of trapped air on the tsunami-induced transient loads and response of coastal bridges. *Geosciences*, 9(4), 191. https://doi.org/10.3390/geosciences9040191.
- Istrati, D., Buckle, I., Lomonaco, P., & Yim, S. (2018). Deciphering the tsunami wave impact and associated connection forces in open-girder coastal bridges. *Journal of Marine Science and Engineering*, 6(4), 1-35. https://doi.org/10.3390/jmse6040148.
- Ma, Z., Zhou, T., Sun, J., & Zhai, G. (2019). Simulation of tsunami-like solitary wave run-up around a conical island using a modified mass source method. *Engineering Applications of Computational Fluid Mechanics*, *13*(1), 849-859. https://doi.org/10.1080/19942060.2019.1642960.
- Menezes, E.J.N., Araújo, A.M., & Da Silva, N.S.B. (2018). A review of wind turbine control and its associated methods. *Journal of Cleaner Production*, 174, 945-953. https://doi.org/10.1016/j.jclepro.2017.10.297.
- Milles, A., Merabet, E., Benbouhenni, H., Colak, I., Bensedira, N., Debdouche, N., Aggoune, M.-S., Boukhalfa, G. (2025). Enhancing the backstepping control approach competencies for wind turbine systems using a dual star induction generator. *Scientific Reports*, 15(1), 1-30. https://doi.org/10.1038/s41598-025-97771-0.
- Moideen, R., Ranjan, B.M., Kamath, A., & Bihs, H. (2019). Effect of girder spacing and depth on the solitary wave impact on the coastal bridge deck for different air gaps. *Journal of Marine Science and Engineering*, 7(5), 140. https://doi.org/10.3390/jmse7050140.
- Motamedi, N.A., Farhi, M.M., & Davoudi, L. (2017). Effect of coastal forest on solitary breaking waves force absorption in sloping coasts. *Journal of Irrigation Sciences and Engineering*, 40(2), 251-263. https://sid.ir/paper/217309/en.
- Narayana, A.C., Tatavarti, R., & Shakdwipe, M. (2005). Tsunami of 26 December 2004: observations on the Kerala coast. *Journal of the Geological Society of India*, 65(2), 239-246.
- Rajendran, S., & Jena, D. (2014). Control of variable speed variable pitch wind turbine at above and below rated wind speed. *Journal of Wind Energy*, 2014(1), 709128. https://doi.org/10.1155/2014/709128.
- Ramsden, J.D. & Raichlen, F. (1990). Forces on vertical wall caused by incident bores. *Journal of Waterway, Port, Coastal, and Ocean Engineering*, 116(5), 592-613. https://doi.org/10.1061/(ASCE)0733-950X(1990)116:5(592).
- Ramsden, J.D. (1996). Forces on a vertical wall due to long waves, bores, and dry-bed surges. *Journal of Waterway, Port, Coastal, and Ocean Engineering*, 122(3), 134-141. https://doi.org/10.1061/(ASCE)0733-950X(1996)122:3(134).
- Ren, B., Liu, M., Li, X.-l., & Wang, Y.-x. (2016). Experimental investigation of wave slamming on an open structure supported elastically. *China Ocean Engineering*, 30, 967-979. https://doi.org/10.1007/s13344-016-0063-1.
- Robertson, I.N., Paczkowski, K., Riggs, H.R., & Mohamed, A. (2013). Experimental investigation of tsunami bore forces on vertical walls. *Journal of Offshore Mechanics and Arctic Engineering*, 135(2), 1-8. https://doi.org/10.1115/1.4023149.
- Roussos, A.I., Ntampasi, V.E., & Kosmidou, O.I. (2013). Pitch control for variable speed wind turbines. In *Proceedings of the 10th International Conference on Informatics in Control, Automation and Robotics* (Vol. 2, pp 43-49). INSTICC. Reykjavík, Iceland. https://doi.org/10.5220/0004391000430049.
- Samantaray, S., Sahoo, P., Sahoo, A., & Satapathy, D.P. (2023). Flood discharge prediction using improved ANFIS model combined with hybrid particle swarm optimisation and slime mould algorithm, *Environmental Science and Pollution Research*, 30(35), 83845-83872. https://doi.org/10.1007/s11356-023-27844-y.
- Soriano, L.A., Yu, W., & Rubio, J.d.J. (2013). Modelling and control of a wind turbine. *Mathematical Problems in Engineering*, 2013(1), 1-13. https://doi.org/10.1155/2013/982597.
- Stansberg, C.T. (2020). Wavefront steepness and influence on horizontal deck impact loads. *Journal of Marine Science and Engineering*, 8(5), 1-24. https://doi.org/10.3390/jmse8050314.



- Talpur, N., Salleh, M.N.M., Hussain, K., & Ali, H. (2019). Modified ANFIS with Less model complexity for classification problems. In: Omar, S., Suhaili, W.S.H., Phon-Amnuaisuk, S. (eds) *Computational Intelligence in Information Systems*. Springer International Publishing, pp. 36-47. https://doi.org/10.1007/978-3-030-03302-6 4.
- Yeh, H., & Sato, S. (2016). Tsunami effects on buildings and coastal structures. *Journal of Disaster Research*, 11(4), 662-669. https://doi.org/10.20965/jdr.2016.p0662.
- Zeng, C.F., Xue, X.L., Zheng, G., Xue, T.Y., & Mei, G.X. (2018). Responses of retaining wall and surrounding ground to pre-excavation dewatering in an alternated multi-aquifer-aquitard system. *Journal of Hydrology*, 559(2), 609-626. https://doi.org/10.1016/j.jhydrol.2018.02.069.
- Zolkifly, M.Z., Nayan, N.M., Abdullah, A.N., Mazalan, S.K., Isa, Z.M., Arshad, M.H. (2018). Cascaded micro wind turbine braking mechanism via dynamic braking and yaw control. *Journal of Telecommunication, Electronic and Computer Engineering*, 10(1-14), 7-14.



Original content of this work is copyright © Ram Arti Publishers. Uses under the Creative Commons Attribution 4.0 International (CC BY 4.0) license at https://creativecommons.org/licenses/by/4.0/

Publisher's Note- Ram Arti Publishers remains neutral regarding jurisdictional claims in published maps and institutional affiliations.